

1 **OH measurements in the coastal atmosphere of South China: Possible missing OH sinks in aged**
2 **air masses**

3
4 Zhouxing Zou¹, Qianjie Chen¹, Men Xia¹, Qi Yuan¹, Yi Chen², Yanan Wang¹, Enyu Xiong¹, Zhe Wang²,
5 and Tao Wang^{1*}

6
7 ¹Department of Civil and Environmental Engineering, The Hong Kong Polytechnic University, Hong
8 Kong, China

9 ²Division of Environment and Sustainability, The Hong Kong University of Science and Technology,
10 Hong Kong, China

11
12 Correspondence to:

13 Tao Wang (tao.wang@polyu.edu.hk)

14
15 **Abstract**

16 The hydroxyl radical (OH) is the main oxidant responsible for the removal of many reduced trace gases
17 and the formation of secondary air pollutants. However, due to technical difficulties in measuring OH,
18 the existing measurements of atmospheric OH concentrations are limited, and its sources and sinks are
19 not well understood under low NO_x conditions. In this study, we observed the OH concentrations using
20 chemical ionization mass spectrometry at a coastal site in Hong Kong from October to November 2020.
21 The average noontime OH concentration over the study period was measured at $4.9 \pm 2.1 \times 10^6 \text{ cm}^{-3}$.
22 We found that a box model with comprehensive observational constraints reproduced the observed
23 daytime OH concentrations when air parcels originated from the continental regions. However, this
24 model overpredicted the observed daytime OH concentrations for coastal air parcels by 142% on
25 average. The missing OH reactivity, which is defined as the OH loss from unmeasured trace gases, is
26 proposed to be the cause of this overprediction. The estimated missing OH reactivity was found in the
27 case of low concentrations of nitrogen oxides (NO_x) and volatile organic compounds, as well as in aged
28 air, and we hypothesize that there could be unmeasured chemical species that cause the model to
29 overestimate OH in aged coastal air parcels. Further studies are needed to find out the exact cause of

1 the model overestimation and to identify the suspected unmeasured chemical species that contribute to
2 the OH budget, in order to better quantify the formation of secondary air pollutants.

3 4 **1. Introduction**

5 The hydroxyl radical (OH) dominates atmospheric oxidative capacity and participates in nearly all
6 sunlit tropospheric chemistry. The primary sources of the ambient OH radical include the photolysis of
7 ozone (O₃) and nitrous acid (HONO) and the ozonolysis of alkenes. The OH sinks are mainly the
8 reactions of OH with trace gases, including carbon monoxide (CO), sulfur dioxide (SO₂), nitric oxide
9 (NO), nitrogen dioxide (NO₂), methane, and other volatile organic compounds (VOCs, Fuchs et al.,
10 2018). In reactions with CO and VOCs, peroxy radicals (HO₂ and RO₂) are produced and then recycled
11 back into OH in the presence of NO as a secondary OH source. This interconversion is closely related
12 to photochemical smog production (Stone et al., 2012). The reaction of OH with SO₂ and NO₂ produces
13 H₂SO₄ and HNO₃, contributing to new particle formation and the acidity of rain, fog, and aerosols. OH
14 also plays an important role in the climate system through reactions with the greenhouse gas CH₄ and
15 the sulfate aerosol precursor dimethyl sulfide (DMS)(Berresheim et al., 2002).

16
17 Measuring ambient OH is challenging due to its high reactivity, short lifetime (< 1 s), and low
18 environmental concentration (Stone et al., 2012). After decades of efforts, tropospheric OH radicals can
19 now be detected following the development of laser-induced fluorescence (LIF)–fluorescence assay
20 with gas expansion (Heard and Pilling, 2003), chemical ionization mass spectrometry (CIM, Eisele and
21 Tanner, 1991), and open-path differential optical absorption spectrometry (Hausmann et al., 1997). The
22 theory, advantages, and disadvantages of various measuring techniques have been discussed previously
23 (Heard and Pilling, 2003; Mao et al., 2012). Using these techniques, multiple campaigns have been
24 conducted to measure the atmospheric OH concentrations in different regions around the globe. Figure
25 S1 and Table S1 summarise the previous field observations of OH radicals in various environments.

26
27 The OH observations are often compared with model simulations to evaluate whether a model has
28 included the major OH sources and sinks. A summary of the results of the most recent studies is shown
29 in Table S1 with the simulation to observation ratios ($R_{S/O}$). As concluded in previous reviews (Stone et

1 al., 2012; Rohrer et al., 2014; Lu et al., 2019), observed OH concentrations can generally be reproduced
2 by box models under high NO conditions ($\text{NO} > 1$ ppb), such as at urban sites or within polluted air
3 masses (Shirley et al., 2006; Griffith et al., 2016; Slater et al., 2020). However, discrepancies between
4 model predictions and observations have often been found under low NO conditions ($\text{NO} < 1$ ppb). The
5 model typically overpredicts OH concentrations in a low VOC environment and underpredicts them in
6 a high biogenic VOC (BVOC) environment, as discussed below.

7
8 The model overestimation of OH has been found in remote marine boundary layers and coastal, urban,
9 and Arctic regions (Table S1), which is attributed to the overestimation of OH sources, missing OH
10 sinks, or the uncertainties inherent in model simulation and observation. For example, model
11 overestimation of OH has been found when dominant sources, such as HONO (in the Antarctic, Kukui
12 et al., 2014a) and HO_2 (in the coastal area Kanaya et al., 2007), are overestimated. In these cases, the
13 overestimation of OH was resolved when these sources were better constrained in the model.
14 Unmeasured VOCs have been proposed as the missing OH sinks, resulting in the overestimation of OH,
15 e.g., in aged air in Idaho Hill (McKeen et al., 1997), in the marine boundary layer (MBL) of Mace
16 Head (Carslaw et al., 1999; Berresheim et al., 2002), in the MBL in Tasmania (Creasey et al., 2003),
17 in Antarctica (Mauldin III et al., 2010), and the urban area of California (Griffith et al., 2016). Other
18 studies have shown evidence of missing OH sinks in various types of environments (Lou et al., 2010;
19 Yang et al., 2016), e.g., in the clean forest (Hansen et al., 2014) and marine (Thames et al., 2020) areas,
20 which is likely resulted from unmeasured organic compounds emitted from biogenic (Kaiser et al., 2016)
21 or oceanic (Thames et al., 2020) sources and their oxidation products. A few studies have shown that
22 the overestimations fall within measurement uncertainties of DOAS, CIMS (McKeen et al., 1997), and
23 LIF, (Carslaw et al., 1999) while others have suggested a possible sampling loss of OH in CIMS
24 (Mauldin III et al., 2010) or a possible calibration bias due to low relative humidity (CIMS, Mauldin III
25 et al., 2001).

26
27 Underestimations of OH by models have mostly been found in forest areas with high BVOC emissions
28 and low NO conditions. Few recent studies also found the OH estimation in urban atmospheres when
29 the NO level was below 1ppb (Whalley et al., 2018; Tan et al., 2017, 2019). These underestimations

1 have usually been attributed to missing OH sources (Tan et al., 2001; Lelieveld et al., 2008;
2 Hofzumahaus et al., 2009; Whalley et al., 2011). To explain the missing sources in forested regions, a
3 series of new OH regeneration reactions under low NO conditions were proposed based on chamber
4 experiments that investigated the oxidation of isoprene by OH. This mechanism, known as the Leuven
5 isoprene mechanism (LIM1; Peeters et al., 2014), includes unimolecular reactions (Peeters et al., 2009;
6 da Silva et al., 2010; Fuchs et al., 2013; Novelli et al., 2020) and isomerization of isoprene and/or its
7 products (Peeters and Müller, 2010; Fuchs et al., 2014). With the adoption of this mechanism, the
8 simulated OH concentration increased by 20% – 30% in the forest region (Lew et al., 2020). Another
9 breakthrough was the development of a new chemical scavenging technique in LIF instruments that
10 were able to determine the interference to the instrument's background. Some studies have shown that
11 the interference in LIF instruments can partly explain the previously observed high OH concentrations
12 (Mao et al., 2012; Hens et al., 2014; Novelli et al., 2014; Feiner et al., 2016; Woodward-Massey et al.,
13 2020). With the adoption of interference scavenging and the LIM1 improved mechanism, measurements
14 using LIF in an Alabama forest (Feiner et al., 2016) and CIMS in Amazon forests (Jeong et al., 2022)
15 agreed with the OH concentration predicted by the model. However, the models in other studies
16 continued to underestimate OH with the improved mechanism (Tan et al., 2019; Lew et al., 2020).

17
18 The industrialization of the Pearl River Delta (PRD) region of south China over the past three decades
19 has been accompanied by high anthropogenic emissions of air pollutants (Lu et al., 2013), causing
20 elevated concentrations of surface ozone (Wang et al., 2019b) and particulate matter (Yao et al., 2014).
21 Measurements of OH in the PRD region that were taken using LIF at a forested site (Backgarden)
22 indicated missing OH sources at this BVOC-rich site (Hofzumahaus et al., 2009; Lu et al., 2012). More
23 recently, OH concentrations were measured at a suburban site in Shenzhen during the autumn of 2018
24 (Wang et al., 2019a, 2021a) using a newly developed LIF instrument. The OH concentrations, which
25 had an average value of $5.3 \times 10^6 \text{ cm}^{-3}$ around noon, were briefly presented with no comparison to
26 modeled OH.

27
28 In the present study, we measured OH concentrations using quadrupole CIMS from October to
29 November 2020 at a background site in Hong Kong. The study aimed to determine the OH

1 concentrations in coastal south China and to investigate whether they could be simulated by a state-of-
2 the-art chemical model under different airflow conditions. We first give a brief description of the site
3 and OH measurement procedure, including the working theory of CIMS, calibration, uncertainties, and
4 modelling setup. We then present the overall measurement results for different air masses and compare
5 them with those found in previous studies. After this, we simulate OH concentrations using a box model
6 constrained by comprehensive observations and discuss possible reasons for the model–observation
7 discrepancy. Our measurements add to the limited database of ambient OH radical concentrations, while
8 our analysis sheds light on possible missing OH sinks under low NO_x conditions.

9 10 **2. Methodology**

11 **2.1 The Hok Tsui Supersite**

12 The field campaign was conducted at the Cape D’Aguilar (also known as Hok Tsui, HT) Air Quality
13 Supersite, which is operated by the Hong Kong Environmental Protection Department, between 6
14 October and 24 November 2020. The HT Supersite (22°12'32" N, 114°15'12" E) is a coastal site located
15 at the south-eastern tip of Hong Kong Island. The site is surrounded by ocean, vegetation, and a country
16 road (Figure 1) and is around 15 km away from the nearest urban center. There is no strong
17 anthropogenic emission source in the surrounding area apart from the ocean-going vessels traveling in
18 nearby waters (Peng et al., 2022). Nonetheless, the site does occasionally receive polluted air masses
19 from mainland China, including air masses from the highly urbanized PRD region (Li et al., 2018; Peng
20 et al., 2022).

21
22 We measured OH radicals, O₃, NO_x, CO, HONO, VOCs, oxygenated VOCs (OVOCs), relative humidity,
23 temperature, NO₂ photolysis frequency (J_{NO_2}), and aerosol size distribution. Table 1 summarises the
24 measurement technique, resolution, and detection limits. The OH-CIMS was housed in an air-
25 conditioned shelter in yard B together with the time-of-flight (ToF)-CIMS and ozone and NO_x analyzers
26 (Figure 1). J_{NO_2} was measured on top of the shelter. The other species and the aerosol size distribution
27 were measured inside the main station building in yard A, which was located around 10 m away from
28 yard B (Figure 1). The backward trajectory was calculated at 1-hour intervals on sampling days at an
29 elevation of 60 m above ground level using the MeteoInfoMap software package (meteothink.org, Wang,

1 2014, 2019).

2

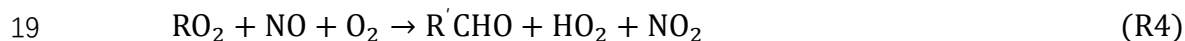
3 **2.2 OH radical measurements**

4 OH radical concentrations were indirectly measured using a custom-built quadrupole CIMS instrument
5 (THS Inc, Atlanta). The THS CIMS was originally developed by (Eisele and Tanner, 1991) and
6 improved upon in subsequent works (Eisele and Tanner, 1993; Tanner and Eisele, 1995; Tanner et al.,
7 1997). The ambient OH concentrations were measured by first converting the OH (by addition of SO₂)
8 to sulfuric acid (H₂SO₄) which was further converted to HSO₄⁻ ion followed by its detection with a
9 quadrupole mass detector.

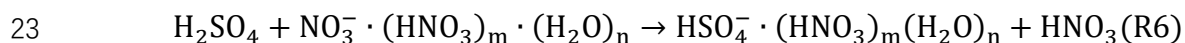
10 A schematic diagram of our OH-CIMS instrument is shown in Figure 2. Ambient air was drawn into
11 the stainless steel inlet with a turbulence-reducing scoop by the inlet pump. The central part of the air
12 in the stainless steel inlet was then drawn into the sample inlet, where OH was converted into H₂SO₄
13 by adding SO₂ to the sample flow (R1 to 3).



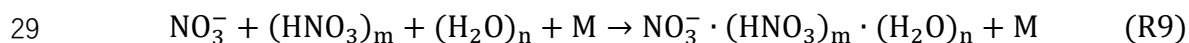
17 The conversion was ended by the addition of scavenger gases (C₃F₆) in the rear flow. The reaction time
18 for OH conversion is 47ms which is short enough to mitigate the HO₂ and RO₂ recycling interference.



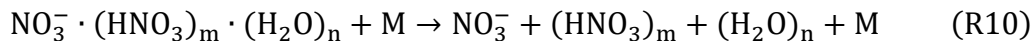
21 The converted H₂SO₄ in the sample flow was then reacted with the excess NO₃⁻ cluster in the sheath
22 flow and converted into an HSO₄⁻ ion cluster in the ionization chamber (R4).



24 The NO₃⁻ reagent ion cluster (NO₃⁻ · (HNO₃)_m · (H₂O)_n) with m and n mostly of 0-2 and 0-3
25 (Berresheim et al., 2000) was generated by passing an HNO₃ containing sheath flow through a ²¹⁰Po
26 ion source (R7 to 9).



1 Where e^- is emitted from the ^{210}Po ion source. The NO_3^- and HSO_4^- ion clusters further dissociated
2 in the collisional dissociation chamber (CDC), refocused in the ion guide chamber (IGC), and were then
3 detected by the detector in the ion detection chamber (IDC).



6 The HSO_4^- and NO_3^- were detected by the peak intensities at $m/z = 97$ (S_{97}) and $m/z = 62$ (S_{62}). The
7 HSO_4^- ion concentration was determined based on relative signal strength (the S_{97}/S_{62} ratio) rather than
8 absolute signal (S_{97}) (Berresheim et al., 2000).

9
10 Apart from ambient OH, some interference gases, such as ambient H_2SO_4 , Criegee intermediates, and
11 artificial OH produced by the ion source, can also be converted into HSO_4^- and contribute to the signal
12 S_{97} . To mitigate such interference, the scavenger gas (C_3F_6) and N_2 were added to the sample flow
13 through electrically operated valves (see the pulsed flow in Figure 2) that automatically switched
14 injection positions every 3 min. When a scavenger gas is added to the front injectors, ambient OH
15 radicals are eliminated by the scavenger instead of reacting with SO_2 due to the higher concentration
16 (~ 100 times) and the faster reaction of C_3F_6 than of SO_2 in the sample flow (Dubey et al., 1996). This
17 allows the background signal (BS_{97}) contributed by the interference gases and instrument noise signal
18 to be determined. When the pulsed flow scavenger gas is switched to the rear injector, the ambient OH
19 radicals and interference gases react with SO_2 to give the total signal (TS_{97}). Then, the ambient OH
20 signal can be obtained by subtracting the signal contributed by interference (BS_{97}) from the total signal
21 (TS_{97}). The measured OH concentration ($[\text{OH}]$) can be calculated using the following equation (E1):

$$22 \quad [\text{OH}] = \frac{1}{C} \times \frac{\text{TS}_{97} - \text{BS}_{97}}{S_{64}} \quad (\text{E1})$$

23 where C is the calibration factor obtained from calibration that was performed using the calibrator
24 shown in Figure 2. The calibration is based on the production of OH radicals through the photolysis of
25 water vapor by 184.9 nm light in the airflow through the calibrator (SR1). The OH concentration
26 produced by the calibrator is calculated by photon flux (I) and H_2O concentration in the airflow (SE1).
27 Calibration was carried out at least every two days during the campaign, as well as before and after any
28 changes in settings. The difference in calibration factors was included in the calibration accuracy.

1 The detection limit was calculated by the background signal as shown by the equation in supplementary
2 (SE3). The detection limit is approximately $1.5 \times 10^5 \text{ cm}^{-3}$ (signal-to-noise ratio of 2) in the laboratory.
3 Due to variations in the concentrations of H_2SO_4 and other interference gases in the ambient air, the
4 background signal during ambient measurement has a larger variation compared to the lab condition,
5 resulting in a higher detection limit in the ambient condition. During the field study, the daytime and
6 night-time average detection limits in this campaign were $1.0 \times 10^6 \text{ cm}^{-3}$ and $0.7 \times 10^6 \text{ cm}^{-3}$, respectively.
7 The overall calibration accuracy was estimated at 38%, by calculation that took into account the
8 uncertainty of all of the parameters measured during the calibration process. The averaged overall
9 uncertainty for this campaign is 44% for OH measurement with consideration of the calibration
10 accuracy and the variations in m/z at 62 (S_{64} , 18%) and at 97 (TS_{97} - BS_{97} , 13%) during observation (SE4
11 and SE5). The technical details and specifications are in Table S2 and the detailed descriptions of CIMS
12 optimization, calibration process, and calculation of detection limit are in the Supplementary
13 Information.

14 **2.3 Box modeling**

15 The Framework for 0-D Atmospheric Modelling (F0AM) using the Master Chemical Mechanism
16 (MCM) v3.3.1 (Wolfe et al., 2016) was used to simulate OH concentrations. MCM v3.3.1
17 (<http://mcm.leeds.ac.uk/MCM>) is a near-explicit chemical mechanism that includes over 17,000
18 elementary reactions of 6700 primary, secondary, and radical species (Jenkin et al., 2015). The isoprene
19 degradation mechanisms, and in particular the mechanisms OH regenerated by HO_x recycling in low
20 NO_x condition, were improved in MCM v3.3.1. The MCM mechanism has been used in previous studies
21 to investigate OH chemistry in different environments, including forests (Stone et al., 2011), urban areas
22 (Slater et al., 2020), suburban areas (Tan et al., 2018), and coastal regions (Sommariva et al., 2004). In
23 our study, observational data (shown in Table S1) were used to constrain the model. These data included
24 VOCs, OVOCs, SO_2 , NO_x , CO, O_3 , HONO, photolysis frequency of NO_2 (J_{NO_2}), and meteorological
25 parameters (temperature, relative humidity, and pressure). The photolysis frequencies for other species
26 were calculated by the “HYBRID” method in F0AM which is based on Tropospheric Ultraviolet and
27 Visible (TUV v5.2) Radiation Model from National Center for Atmospheric Research. The Ozone
28 column we used for TUV calculation was 240 DU (the Dobson unit) which is the average number from
29 October to November 2020 for the Hok Tsui area according to the worldview website ([EOSDIS](https://worldview.earthdata.nasa.gov/))

1 [Worldview \(nasa.gov\)](https://worldview.nasa.gov). The simulated photolysis frequencies were then scaled by the correction factor
2 obtained from the comparison between observed and modeled J_{NO_2} . The first-order physical loss process,
3 with a 24-hour lifetime for all species, was included in the model to represent physical processes (Wolfe
4 et al., 2016; Chen et al., 2022). The physical loss process has a negligible influence on OH simulation
5 because the OH concentrations are controlled by fast *in situ* chemistry.

6
7 The heterogeneous uptake of HO_2 by aerosols was included in the model by assuming a pseudo-first-
8 order loss of HO_2 (E2–E4; Jacob, 2000):

$$\frac{d[\text{HO}_2]}{dt} = -k_{\text{HO}_2}[\text{HO}_2] \quad (\text{E2})$$

$$k_{\text{HO}_2} = \frac{V_{\text{HO}_2} \times S_a \times \gamma_{\text{HO}_2}}{4} \quad (\text{E3})$$

$$V_{\text{HO}_2} = \sqrt{\frac{8RT}{\pi \times MM_{\text{HO}_2}}} \quad (\text{E4})$$

12 where k_{HO_2} is the first-order loss rate coefficient of HO_2 by aerosol uptake, γ_{HO_2} is the effective HO_2
13 uptake coefficient (0.1 for the base model run; Guo et al., 2019), V_{HO_2} is the mean molecular velocity
14 of HO_2 , S_a is the aerosol surface area concentration measured by a scanning mobility particle sizing
15 (SMPS), and MM_{HO_2} (= 17 g/mol) is the molecular mass of HO_2 . We assumed in the model that the
16 products of heterogeneous HO_2 loss would not participate in further reactions (Guo et al., 2019).

17
18 The observation data were averaged every 10 mins for the model input. Any missing values were
19 calculated assuming linear interpolation. The measured concentrations of NO and NO_2 were used to
20 constrain the model. Due to the clean condition of the coastal air, some of the reactive alkenes and long-
21 chain alkanes were below detection limits. For the simulation of those compounds, we used
22 concentrations that were half of the detection limits. The measured VOCs were further divided into
23 those of anthropogenic origin (AVOCs) and biogenic origin (BVOCs). The AVOCs included alkanes
24 (C_2 – C_8), alkenes (C_2 – C_6) benzene, and TEXs (toluene, ethylbenzene, and xylenes), which covered the
25 dominant species originating from petroleum gas and industrial solvent evaporation (Tang et al., 2008),
26 while the BVOCs included isoprene, terpene, pinene, and limonene. The majority (> 95%) of the
27 measured OVOCs in this study were C_1 – C_3 aldehydes, ketones, and acids. For each run, a three-day
28 spin-up was performed with constant photolysis and deposition to create a stable model environment

1 and to avoid the uncertainty of unconstrained species (Carslaw et al., 1999).

3. Results and Discussion

3.1 Overview of observations

5 Figure 3 shows the time series of observed OH concentrations, along with the concentrations of other
6 trace gases and the meteorological parameters, during the study period. The weather conditions featured
7 relatively high temperatures, high relative humidity (RH), and strong solar radiation, similar to previous
8 autumn observations at the same site (Li et al., 2018; Peng et al., 2022). The air temperature ranged
9 from 20°C to 30°C and RH ranged from 40% to 96%. The photolysis frequency of NO₂ (J_{NO_2}) peaked
10 at $8 \times 10^{-3} \text{ s}^{-1}$ around noon on sunny days and decreased to $2 \times 10^{-3} \text{ s}^{-1}$ on cloudy days. The observed
11 OH concentrations were mostly above the detection limit during the daytime but fell closer to the
12 detection limit at night. The OH concentrations showed a distinct diurnal pattern and a positive
13 correlation with J_{NO_2} and calculated $J_{\text{O}_1\text{D}}$ ($R^2 = 0.68$ and 0.46 for J_{NO_2} and calculated $J_{\text{O}_1\text{D}}$, respectively ,
14 Figure S2). The daily maximum OH concentration varied from $2.1 \times 10^6 \text{ cm}^{-3}$ on 21 November,
15 accompanying the lowest level of solar radiation, to $15.4 \times 10^6 \text{ cm}^{-3}$ on 7 November during a pollution
16 episode. The pollution episode began on the evening of 6 November and featured a maximum
17 concentration of 174.0 ppb O₃, 8.7 ppb NO, 22.7 ppb NO₂, 9.8 s⁻¹ total measured VOCs reactivity, and
18 5.8 s⁻¹ total measured OVOCs reactivity. The OH concentration peaked the next day (7 Nov). This
19 suggests abundant OH sources and fast radical propagation under high-NO_x and high-VOC conditions.

21 Figure 4 shows the average diurnal profiles of OH and other representative species. On average, the
22 maximum OH concentration was $4.9 \pm 2.1 \times 10^6 (1\sigma) \text{ cm}^{-3}$. As shown in Table S1, the OH concentrations
23 at our site were comparable to those reported in previous field studies conducted at tropical coastal sites.
24 For example, the reported OH maximum concentration was $4.5 \times 10^6 \text{ cm}^{-3}$ in the low-altitude remote
25 tropical troposphere (Brune et al., 2020). In a study conducted in autumn at a suburban site in Shenzhen,
26 approximately 50 km away from our site, an OH diurnal maximum concentration of $5.3 \times 10^6 \text{ cm}^{-3}$ was
27 observed (Wang et al., 2021b). The averaged night-time OH concentrations in this study was 5.1 ± 1.8
28 $\times 10^5 (1\sigma) \text{ cm}^{-3}$ which was comparable to the previous night-time results (below $10 \times 10^5 \text{ cm}^{-3}$) measured
29 at the PRD region (in Heshan, Tan et al., 2019, and in PKUSZ sites, Yang et al., 2022). The OH

1 concentration was slightly higher in the evening at $6.8 \pm 1.1 \times 10^5$ (1σ) cm^{-3} than in the morning at 3.7
2 $\pm 0.7 \times 10^5$ (1σ) cm^{-3} which might be due to the higher ozone concentration in the evening which leads
3 to a higher OH production from alkene ozonolysis.

4
5 Figure 4 also shows the average diurnal patterns of the other trace gases measured. As a primary source
6 of OH, HONO, peaked in the morning at 0.21 ± 0.09 ppb around 7:00 local time (LT), and O_3 peaked
7 in the afternoon at 70 ± 20 ppb at around 16:00 LT. The average NO and NO_2 concentrations reached a
8 maximum of 1.2 ± 1.6 ppb at around 10:00 LT and 4.9 ± 3.2 ppb at around 18:00 LT, respectively.
9 Isoprene showed a diurnal pattern similar to that of J_{NO_2} and OH, peaking at 0.5 ± 0.4 ppb at noon. The
10 average concentrations of all of the measured species during the campaign are shown in Table S3.

11
12 Figure 5 shows the hourly backward trajectories over the whole campaign. Consistent with previous
13 studies conducted at HT in the same season (Li et al., 2018; Peng et al., 2022), the air masses were
14 dominated by continental air masses containing high concentrations of pollutants (Figure 5a) and less
15 polluted coastal air masses (Figure 5c). In this study, we did not encounter oceanic air masses from the
16 south. The average noontime OH concentration was $5.0 \pm 2.2 \times 10^6$ cm^{-3} in the continental air (Figure
17 5b) and $3.3 \pm 1.6 \times 10^6$ cm^{-3} in the coastal air (Figure 5d).

18 19 **3.2 Model–observation comparison**

20 To investigate the performance of the MCM box model in simulating OH chemistry at our site, we
21 selected 4 days featuring the continental air mass (8, 21, 22, and 23 Oct) and 4 days featuring the coastal
22 air mass (25–27 Oct, 5 November) (Figure 6). We also selected 10 October as a specific case due to the
23 shifting continental and coastal air masses within the same day during the daytime. These days were
24 selected for model analysis because they comprised relatively complete chemical data that could be
25 used to constrain the model. The below discussions focus on the comparison of the daytime results since
26 the simulated night-time OH concentration was mostly within the measurement uncertainties and the
27 night-time observations for Oct 08, 23, 27 and Nov. 5 were incomplete as shown in Figure 6.

28 29 **3.2.1 Selected continental air mass cases**

1 Figure 6 shows the comparison between the simulated and observed OH concentrations for the selected
2 cases in the continental and coastal air masses (4 days each). The simulated OH concentrations of the
3 four continental cases (8 October and 21–23 October) were mostly within the OH measurement
4 uncertainty (2σ), with a daytime average $R_{S/O}$ of 1.14 (Figure 7) and a range from 0.99 to 1.18 (Figure
5 6). High NO_x (~ 5 ppb) and VOCs (~ 17 ppb) concentrations were measured on these days (Figure 7,
6 Table S3). Therefore, in the continental polluted air mass, the existing MCM mechanism reproduced
7 the observed OH concentrations well. On these days, the reaction between HO_2 and NO was the
8 dominant OH formation pathway (78%), followed by O_3 photolysis (8%), HONO photolysis (6%), the
9 reaction between ozone and HO_2 (2%), and alkene ozonolysis ($< 2\%$; Table 2 and Figure S3). These
10 results are similar to the findings of previous studies in the PRD conducted during autumn under
11 polluted conditions (Tan et al., 2019). The removal of OH occurs mainly through its reaction with non-
12 methane hydrocarbons (NMHCs; $\sim 63\%$), CO (20%), NO_2 (9%), and CH_4 (4%; Table 2)

13

14 The simulated daytime average and peak HO_2 concentration were $2.1 \pm 1.2 \times 10^8 \text{ cm}^{-3}$ and 4.5×10^8
15 cm^{-3} , respectively, for continental air masses (RUNBase, Figure S4). The peak HO_2 value at our is lower
16 than the result at a clean midlatitude forest area ($10 \times 10^8 \text{ cm}^{-3}$, Lew et al., 2020), and the average
17 daytime value is higher than that measured at polluted urban sites in Beijing (0.3 to $0.4 \times 10^8 \text{ cm}^{-3}$, Ma
18 et al., 2019). The ratio between simulated HO_2 and observed OH ($\text{HO}_2_{\text{SIM}}/\text{OH}_{\text{OBS}}$) was 147 on the
19 daytime average in continental cases.

20

21 The simulated OH reactivity was $8.1 \pm 1.0 \text{ s}^{-1}$ on average for continental air masses (Figure S5a), which
22 is comparable to the OH reactivity measured at suburban sites which ranged from 5 to 30 s^{-1} but lower
23 than that measured at the urban sites which ranged from 10 to 100 s^{-1} and mentioned by Yang et al.,
24 (2016) and references therein.

25

26 **3.2.2 Selected coastal air mass cases**

27 In contrast to the continental air mass cases, the diurnal OH patterns in the coastal air mass category
28 (25–27 October and 5 November) were not well reproduced by the model (Figure 6). The simulated
29 results overestimated the observed OH concentration, with the daytime average $R_{S/O}$ of 2.42 (Figure 7)

1 for these 4 days (range 2.08 to 3.11; Figure 6). The coastal air masses showed statistically significant
2 ($p < 0.05$) lower NO_x (-63%), AVOCs (-47%), BVOCs (-50%), OVOCs (-23%), and CO (-31%)
3 concentrations compared with the continental cases (Figure 7, Table S3). The HO_2 and NO reaction was
4 still the dominant source (69%) of OH in the coastal air masses, like in the continental air mass cases,
5 but in a lower proportion than on continental days due to the lower NO concentration (Table 2 and
6 Figure S3). The other major OH sources were O_3 photolysis (13.8%), HONO photolysis (7%), and the
7 reaction between ozone and HO_2 (4%).

8
9 The simulated daytime average HO_2 concentration was $3.4 \pm 1.7 \times 10^8 \text{ cm}^{-3}$ for the coastal cases
10 (RUNBase, Figure S4), which was $\sim 1.2 \times 10^8 \text{ cm}^{-3}$ higher than the value in the continental polluted air
11 mass. The simulated HO_2 level is comparable to the measured value at a rural site in Heshan (3×10^8
12 cm^{-3} , Tan et al., 2019). The $\text{HO}_{2_SIM}/\text{OH}_{OBS}$ was 218 in coastal cases, higher than the ratio in continental
13 cases. This could be explained by the lower NO concentration in the coastal cases that slows the
14 recycling reaction of HO_2 back to OH (R4 and R5) (Sommariva et al., 2004; Shirley et al., 2006; Chen
15 et al., 2010).

16
17 The simulated OH reactivity was $4.7 \pm 0.58 \text{ s}^{-1}$ on average for the coastal cases (Figure S5b), which was
18 lower than that of the continental polluted air mass ($8.1 \pm 1.0 \text{ s}^{-1}$). As discussed below in Section 3.3,
19 low OH reactivity could have been the cause of the model's overestimation of OH concentrations in the
20 coastal cases. The model's overestimation of OH in coastal air masses indicates gaps in our knowledge
21 about the OH budget in relatively clean conditions with low NO_x and VOCs.

22 23 **3.2.3 The 10 October case day**

24 During the day on 10 October, our site received continental air masses between sunrise and noon and
25 coastal air masses between noon and sunset. This served as another case that could be used to check the
26 model's performance on continental versus coastal air masses within the same day. On 10 October, the
27 $R_{S/O}$ changed from 1.20 in the morning to 2.59 in the afternoon, driven by the air mass drift during
28 continuous measurement without interruption (Figure 8). As with the continental and coastal results
29 shown above, the afternoon of 10 October showed significantly ($p < 0.05$) lower concentrations of NO

1 (-50%), NO₂ (-68%) and the reactivity of AVOCs (-42%), BVOCs (-27%), and OVOCs (-12%)
2 compared with the morning (Table S3). With lower NO, the fraction of OH produced from HO₂ and NO
3 reaction was also lower in the afternoon (65%) than in the morning (73%; Table 2 and Figure S3).
4 Similarly, the simulated total OH reactivity was lower in the afternoon ($7.6 \pm 2.3 \text{ s}^{-1}$ on average) than
5 in the morning ($10.3 \pm 1.6 \text{ s}^{-1}$ on average; Figure S5c). The simulated HO₂ was $3.6 \pm 2.4 \times 10^8 \text{ cm}^{-3}$ in
6 the morning when continental air mass dominated and was $5.6 \pm 1.9 \times 10^8 \text{ cm}^{-3}$ in the afternoon when
7 coastal air mass dominated (RUNBase, Figure S4). The HO_{2,SIM}/OH_{OBS} was 142 in the morning and up
8 to 476 in the afternoon. Again, higher HO₂ concentration and HO_{2,SIM}/OH_{OBS} ratio were shown with
9 low NO concentration.

11 **3.3 Discussion on the model–observation discrepancy**

12 As discussed in the introduction, the model’s overestimation of OH could have been caused by multiple
13 factors, including uncertainties in OH measurements and modelling, overestimation of OH sources, and
14 underestimation of OH sinks. Below, we discuss possible their roles in the study.

16 **3.3.1 Uncertainties in OH measurement and simulation**

17 The OH measurement uncertainties have been calculated as described in Section 2.2 and are shown as
18 the error bars in Figures 5 and 6. The model’s overestimation of OH in coastal air masses exceeded the
19 measurement uncertainties (Figures 6 and 7), and thus, the measurement uncertainty is unlikely to be
20 the main reason for the discrepancy.

21
22 Model uncertainties in our study include the uncertainties in photolysis frequencies correction,
23 uncertainties in the constrained VOCs concentrations when they were below detection limits, and
24 uncertainties from not considering halogen chemistry. On the first possibility, we acknowledge that the
25 correction factor for photolysis frequencies due to cloud presence may be different for different species
26 (Walker et al., 2022), thus, using a single correction factor (based on J_{NO2}) may introduce uncertainty in
27 the model simulations. We think such uncertainty should not be significant because the weather was
28 mostly sunny in the coastal cases. Regarding the uncertainty from the VOCs input, we conducted a
29 sensitivity test to show that the treatment of VOCs that were below the detection limits should have a

1 negligible effect on OH simulation (RUN_{VOC0} and RUN_{VOCDL} in Figure S4). We did not include halogen
2 chemistry in our study as we wanted to compare our results with previous modelling work most of
3 which did not consider halogen chemistry. Our other studies at the same site that did consider the
4 halogen chemistry show a 4% increase in OH concentration from Cl chemistry (Peng et al., 2022) and
5 2.8% from Br chemistry (Xia et al., 2022), which would even increase the model-measurement
6 in the coastal air mass discrepancy.

8 **3.3.2 Overestimation of OH sources**

9 Our calculated OH budgets show that the main sources of OH in the coastal air masses were the HO₂ +
10 NO reaction (69%), O₃ photolysis (14%), HONO photolysis (7%), and the reaction between ozone and
11 HO₂ (4%). In the simulation, NO, HONO, and O₃ were constrained by observations. Could HO₂ be
12 overestimated which would cause overprediction of OH?

13
14 The main HO₂ sources are the VOCs oxidation by OH and the photolysis of OVOCs. In our study,
15 VOCs and OVOCs were more likely under-measured than over-measured, which would underpredict
16 HO₂ rather than overpredicting it. In addition, not including the halogen chemistry would under-
17 simulate HO₂ at this site (Peng et al., 2022; Xia et al., 2022).

18
19 We next examine the possibility of the underestimation of HO₂ sinks as the cause of the overprediction
20 of OH. The major sinks of HO₂ include the reaction of NO to recycle OH, self-reaction to form H₂O₂,
21 and heterogeneous loss by aerosol uptake. The first and second pathways have been considered in the
22 MCM. The heterogeneous uptake of HO₂ onto aerosol was also included in our simulations with an
23 uptake coefficient of 0.1. We conducted a sensitivity run by increasing the aerosol uptake of HO₂
24 (RUN_{γMAX}, Figure S4). Even when we set the uptake coefficient to unity (which is unlikely large), the
25 simulated HO₂ concentration would decrease by 34% and the simulated OH R_{S/O} would decrease to
26 1.73 from 2.42 in the base case. This indicates that the heterogeneous uptake of HO₂ is not the cause of
27 the overestimation of OH in the coastal case. In summary, the discrepancy in modelled and observed
28 OH in coastal cases is unlikely to be due to the overestimated HO₂.

3.3.3 Possible missing OH reactivity.

Based on the above discussions, we propose that the model's overestimation of OH could have been caused by unmeasured species that were not included in the model as OH sinks. We attempt to estimate the magnitude of possible OH sinks and investigate which factors could be important to these sinks. We added an artificial loss reaction into the model with the reactivity of k_{miss} (s^{-1}) and assumed that the reaction product would not participate in further reactions. Assuming a pseudo-steady state of OH during the daytime ($P = k[OH]$), k_{miss} was calculated as follows:

$$k_{miss} = \frac{P_{constrain}}{[OH_{obs}]} - \frac{P_{constrain}}{[OH_{sim}]} \quad (E9)$$

where $P_{constrain}$ is the model's calculated OH production rates, with OH constrained by observations; $[OH_{obs}]$ is the observed OH concentration; and $[OH_{sim}]$ is the OH concentration simulated in RUNBase. After introducing the OH sink with k_{miss} into the model, the model better reproduced the observed OH concentrations on the coastal case days, with daytime $R_{S/O}$ close to unity (RUNKmiss Figure S6). The average daytime k_{miss} for the coastal cases was $5.0 \pm 2.6 s^{-1}$, which larger than the total calculated reactivity in coastal cases ($4.7 \pm 0.58 s^{-1}$). The calculated k_{miss} could be a lower limit of the possible missing source as the products from the reactions of OH with unknown species are most likely to further react with the missing source to produce RO_2 and HO_2 and recycle back to OH.

We next explored the dependence of k_{miss} on different trace gases. Figure 9a shows the correlation between k_{miss} and NO concentration for the nine case days (including 10 October) between 09:00 and 15:00. At $NO > 0.5$ ppb, k_{miss} is close to zero. At $NO < 0.5$ ppb, k_{miss} tended to increase with decreasing NO. Similarly, k_{miss} approached zero at high concentrations of NO_2 (> 2.5 ppb), TEXs (> 0.25 ppb), and AVOCs (> 5 ppb; Figure 9) and increased with decreasing concentrations of NO_2 , TEXs, and AVOCs. High k_{miss} also typically occurred at low toluene/benzene ratios and low C_2H_2/CO ratios (Figure 9), which are indicators of an aged air mass (Xiao et al., 2007; Kuyper et al., 2020).

Therefore, while we cannot completely rule out other possibilities, we argue that the aged coastal air masses could have contained unmeasured species such as oxygenated organic molecules (OOMs; Nie et al., 2022) and ocean-emitted gases (Thames et al., 2020) that contributed to the missing OH reactivity, causing the model to overestimate OH concentrations on the coastal case days.

1
2
3
4
5
6
7
8
9
10
11
12
13
14
15
16
17
18
19
20
21
22
23
24
25
26
27
28

4. Summary and conclusion

In this study, we measured OH concentrations using CIMS at a coastal site in Hong Kong in the autumn of 2020 to gain insights into the atmospheric oxidative capacity and to evaluate the performance of a box model in the coastal atmosphere. The daily maximum OH concentration ranged from 2.1 to $15.4 \times 10^6 \text{ cm}^{-3}$ over the whole campaign, with an average of $4.9 \pm 2.1 \times 10^6 \text{ cm}^{-3}$. The air masses were categorized into two groups based on their backward air trajectories: (1) continental air masses, which contained high concentrations of NO_x and VOCs, and (2) coastal air masses, which contained low concentrations of NO_x and VOCs. The observed OH concentration in the continental air parcels was on average 52% higher than in the coastal air parcels. The F0AM box model with comprehensive observational constraints generally reproduced the observed OH in the continental cases during the daytime, with a simulated/observed OH ratio ($R_{S/O}$) of 1.14 on average. However, the model significantly overestimated OH concentrations in the coastal cases, with an $R_{S/O}$ of 2.42 on average during the daytime. While we cannot completely rule out other possibilities, we incline to attribute this overestimation to a missing OH reactivity in the aged coastal air parcels that were not accounted for in the model. The lower limit of the missing OH reactivity was estimated at $5.0 \pm 2.6 \text{ s}^{-1}$ on average between 09:00 and 15:00 and was especially larger under low NO_x , low AVOCs, and aged air conditions. We hypothesize that unknown products from AVOC oxidation or unknown OH-reacting gases emitted from oceans could contribute to the missing OH reactivity in aged coastal air masses. The overestimation of OH in the model could cause an overestimation of the formation of secondary aerosols, such as sulfate and nitrate, while the impacts would be even more complicated if it is due to missing chemical species which participated in ozone formation. Further studies are necessary to pin down the exact cause(s) of the OH overestimation by concurrently measuring HO_2 and OH reactivities, VOC oxidation products, and ocean-emitted trace gases.

Data availability. All of the data used to produce this paper can be obtained by contacting Tao Wang (two.wang@polyu.edu.hk).

Supplement. The online supplement for this article is available at:

1 **Author contributions.** TW initially conceived the project. TW and ZW planned and organized the
2 overall field campaign at Hok Tsui. ZZ conducted the OH measurements using CIMS, with
3 contributions from TW and ZW. YC performed the aerosol size distribution measurements. YQ
4 performed the OVOC measurements using PTR-MS. MX and YC performed the HONO measurements
5 using ToF-CIMS. YW assisted with HONO calibration. ZZ performed the box model analysis and
6 sensitivity test with contributions from EX and QC. ZZ, TW, and QC analyzed the data and interpreted
7 the results, with contributions from MX. ZZ, TW, and QC wrote the paper. All of the authors reviewed
8 and commented on the paper.

9 **Competing interests.** One author (Tao Wang) is a member of the editorial board of Atmospheric
10 Chemistry and Physics. The peer-review process was guided by an independent editor, and the authors
11 have no other competing interests to declare.

12 **Acknowledgments**

13 We thank David Tanner, Dr. Wei Pu, and Dr. Weihao Wang for developing the OH CIMS. We are also
14 grateful to the Environmental Protection Department of Hong Kong, for loaning the CIMS instrument
15 and providing access to its station and data on trace gases, and to the Hong Kong Observatory, for
16 supplying meteorology data.

17 **Financial support.** This research was financially supported by the Hong Kong Research Grants
18 Council (T24-504/17-N and 15223221).

19

20

1 **Reference:**

- 2 Berresheim, H., Elste, T., Plass-Dülmer, C., Eiseleb, F. L., and Tannerb, D. J.: Chemical ionization mass
3 spectrometer for long-term measurements of atmospheric OH and H₂SO₄, *International Journal of*
4 *Mass Spectrometry*, 202, 91–109, [https://doi.org/10.1016/S1387-3806\(00\)00233-5](https://doi.org/10.1016/S1387-3806(00)00233-5), 2000.
- 5 Berresheim, H., Elste, T., Tremmel, H. G., Allen, A. G., Hansson, H.-C., Rosman, K., Dal Maso, M., Mäkelä,
6 J. M., Kulmala, M., and O'Dowd, C. D.: Gas-aerosol relationships of H₂SO₄, MSA, and OH: Observations
7 in the coastal marine boundary layer at Mace Head, Ireland, *Journal of Geophysical Research:*
8 *Atmospheres*, 107, PAR 5-1-PAR 5-12, <https://doi.org/10.1029/2000JD000229>, 2002.
- 9 Brune, W. H., Miller, D. O., Thames, A. B., Allen, H. M., Apel, E. C., Blake, D. R., Bui, T. P., Commane, R.,
10 Crouse, J. D., Daube, B. C., Diskin, G. S., DiGangi, J. P., Elkins, J. W., Hall, S. R., Hanisco, T. F., Hannun,
11 R. A., Hintsä, E. J., Hornbrook, R. S., Kim, M. J., McKain, K., Moore, F. L., Neuman, J. A., Nicely, J. M.,
12 Peischl, J., Ryerson, T. B., St. Clair, J. M., Sweeney, C., Teng, A. P., Thompson, C., Ullmann, K., Veres, P.
13 R., Wennberg, P. O., and Wolfe, G. M.: Exploring Oxidation in the Remote Free Troposphere: Insights
14 From Atmospheric Tomography (ATom), *JGR Atmospheres*, 125,
15 <https://doi.org/10.1029/2019JD031685>, 2020.
- 16 Carslaw, N., Creasey, D. J., Heard, D. E., Lewis, A. C., McQuaid, J. B., Pilling, M. J., Monks, P. S., Bandy,
17 B. J., and Penkett, S. A.: Modeling OH, HO₂, and RO₂ radicals in the marine boundary layer: 1. Model
18 construction and comparison with field measurements, *J. Geophys. Res.*, 104, 30241–30255,
19 <https://doi.org/10.1029/1999JD900783>, 1999.
- 20 Chen, Q., Xia, M., Peng, X., Yu, C., Sun, P., Li, Y., Liu, Y., Xu, Z., Xu, Z., Wu, R., Nie, W., Ding, A., Zhao,
21 Y., and Wang, T.: Large Daytime Molecular Chlorine Missing Source at a Suburban Site in East China,
22 *JGR Atmospheres*, 127, <https://doi.org/10.1029/2021JD035796>, 2022.
- 23 Chen, S., Ren, X., Mao, J., Chen, Z., Brune, W. H., Lefer, B., Rappenglück, B., Flynn, J., Olson, J., and
24 Crawford, J. H.: A comparison of chemical mechanisms based on TRAMP-2006 field data, *Atmospheric*
25 *Environment*, 44, 4116–4125, <https://doi.org/10.1016/j.atmosenv.2009.05.027>, 2010.
- 26 Creasey, D. J.: Measurements of OH and HO₂ concentrations in the Southern Ocean marine boundary
27 layer, *J. Geophys. Res.*, 108, 4475, <https://doi.org/10.1029/2002JD003206>, 2003.
- 28 Dubey, M. K., Hanisco, T. F., Wennberg, P. O., and Anderson, J. G.: Monitoring potential photochemical
29 interference in laser-induced fluorescence Measurements of atmospheric OH, *Geophys. Res. Lett.*, 23,
30 3215–3218, <https://doi.org/10.1029/96GL03008>, 1996.
- 31 Eisele, F. L. and Tanner, D. J.: Ion-assisted tropospheric OH measurements, *J. Geophys. Res.*, 96, 9295,
32 <https://doi.org/10.1029/91JD00198>, 1991.
- 33 Eisele, F. L. and Tanner, D. J.: Measurement of the gas phase concentration of H₂SO₄ and methane
34 sulfonic acid and estimates of H₂SO₄ production and loss in the atmosphere, *Journal of Geophysical*
35 *Research: Atmospheres*, 98, 9001–9010, <https://doi.org/10.1029/93JD00031>, 1993.
- 36 Feiner, P. A., Brune, W. H., Miller, D. O., Zhang, L., Cohen, R. C., Romer, P. S., Goldstein, A. H., Keutsch,

- 1 F. N., Skog, K. M., Wennberg, P. O., Nguyen, T. B., Teng, A. P., DeGouw, J., Koss, A., Wild, R. J., Brown,
2 S. S., Guenther, A., Edgerton, E., Baumann, K., and Fry, J. L.: Testing Atmospheric Oxidation in an
3 Alabama Forest, *Journal of the Atmospheric Sciences*, 73, 4699–4710, [https://doi.org/10.1175/JAS-](https://doi.org/10.1175/JAS-D-16-0044.1)
4 [D-16-0044.1](https://doi.org/10.1175/JAS-D-16-0044.1), 2016.
- 5 Fuchs, H., Hofzumahaus, A., Rohrer, F., Bohn, B., Brauers, T., Dorn, H.-P., Häsel, R., Holland, F.,
6 Kaminski, M., Li, X., Lu, K., Nehr, S., Tillmann, R., Wegener, R., and Wahner, A.: Experimental evidence
7 for efficient hydroxyl radical regeneration in isoprene oxidation, *Nature Geosci*, 6, 1023–1026,
8 <https://doi.org/10.1038/ngeo1964>, 2013.
- 9 Fuchs, H., Acir, I.-H., Bohn, B., Brauers, T., Dorn, H.-P., Häsel, R., Hofzumahaus, A., Holland, F.,
10 Kaminski, M., Li, X., Lu, K., Lutz, A., Nehr, S., Rohrer, F., Tillmann, R., Wegener, R., and Wahner, A.: OH
11 regeneration from methacrolein oxidation investigated in the atmosphere simulation chamber
12 SAPHIR, *Atmos. Chem. Phys.*, 14, 7895–7908, <https://doi.org/10.5194/acp-14-7895-2014>, 2014.
- 13 Fuchs, H., Albrecht, S., Acir, I., Bohn, B., Breitenlechner, M., Dorn, H.-P., Gkatzelis, G. I., Hofzumahaus,
14 A., Holland, F., Kaminski, M., Keutsch, F. N., Novelli, A., Reimer, D., Rohrer, F., Tillmann, R., Vereecken,
15 L., Wegener, R., Zaytsev, A., Kiendler-Scharr, A., and Wahner, A.: Investigation of the oxidation of
16 methyl vinyl ketone (MVK) by OH radicals in the atmospheric simulation chamber SAPHIR, *Atmos.*
17 *Chem. Phys.*, 18, 8001–8016, <https://doi.org/10.5194/acp-18-8001-2018>, 2018.
- 18 Griffith, S. M., Hansen, R. F., Dusanter, S., Michoud, V., Gilman, J. B., Kuster, W. C., Veres, P. R., Graus,
19 M., Gouw, J. A., Roberts, J., Young, C., Washenfelder, R., Brown, S. S., Thalman, R., Waxman, E.,
20 Volkamer, R., Tsai, C., Stutz, J., Flynn, J. H., Grossberg, N., Lefer, B., Alvarez, S. L., Rappenglueck, B.,
21 Mielke, L. H., Osthoff, H. D., and Stevens, P. S.: Measurements of hydroxyl and hydroperoxy radicals
22 during CalNex-LA: Model comparisons and radical budgets, *J. Geophys. Res. Atmos.*, 121, 4211–4232,
23 <https://doi.org/10.1002/2015JD024358>, 2016.
- 24 Guo, J., Wang, Z., Tao Wang, and Zhang, X.: Theoretical evaluation of different factors affecting the
25 HO₂ uptake coefficient driven by aqueous-phase first-order loss reaction, *Science of The Total*
26 *Environment*, 683, 146–153, <https://doi.org/10.1016/j.scitotenv.2019.05.237>, 2019.
- 27 Hansen, R. F., Griffith, S. M., Dusanter, S., Rickly, P. S., Stevens, P. S., Bertman, S. B., Carroll, M. A.,
28 Erickson, M. H., Flynn, J. H., Grossberg, N., Jobson, B. T., Lefer, B. L., and Wallace, H. W.: Measurements
29 of total hydroxyl radical reactivity during CABINEX 2009 – Part 1: field measurements, *Atmos. Chem.*
30 *Phys.*, 14, 2923–2937, <https://doi.org/10.5194/acp-14-2923-2014>, 2014.
- 31 Hausmann, M., Brandenburger, U., Brauers, T., and Dorn, H.-P.: Detection of tropospheric OH radicals
32 by long-path differential-optical-absorption spectroscopy: Experimental setup, accuracy, and
33 precision, *J. Geophys. Res.*, 102, 16011–16022, <https://doi.org/10.1029/97JD00931>, 1997.
- 34 Heard, D. E. and Pilling, M. J.: Measurement of OH and HO₂ in the Troposphere, *Chem. Rev.*, 103,
35 5163–5198, <https://doi.org/10.1021/cr020522s>, 2003.
- 36 Hens, K., Novelli, A., Martinez, M., Auld, J., Axinte, R., Bohn, B., Fischer, H., Keronen, P., Kubistin, D.,
37 Nölscher, A. C., Oswald, R., Paasonen, P., Petäjä, T., Regelin, E., Sander, R., Sinha, V., Sipilä, M.,

- 1 Taraborrelli, D., Tatum Ernest, C., Williams, J., Lelieveld, J., and Harder, H.: Observation and modelling
2 of HO_x radicals in a boreal forest, *Atmospheric Chemistry and Physics*, 14, 8723–8747,
3 <https://doi.org/10.5194/acp-14-8723-2014>, 2014.
- 4 Hofzumahaus, A., Rohrer, F., Lu, K., Bohn, B., Brauers, T., Chang, C.-C., Fuchs, H., Holland, F., Kita, K.,
5 Kondo, Y., Li, X., Lou, S., Shao, M., Zeng, L., Wahner, A., and Zhang, Y.: Amplified Trace Gas Removal
6 in the Troposphere, *Science*, 324, 1702–1704, <https://doi.org/10.1126/science.1164566>, 2009.
- 7 Jacob, D.: Heterogeneous chemistry and tropospheric ozone, *Atmospheric Environment*, 34, 2131–
8 2159, [https://doi.org/10.1016/S1352-2310\(99\)00462-8](https://doi.org/10.1016/S1352-2310(99)00462-8), 2000.
- 9 Jenkin, M. E., Young, J. C., and Rickard, A. R.: The MCM v3.3.1 degradation scheme for isoprene, *Atmos.*
10 *Chem. Phys.*, 15, 11433–11459, <https://doi.org/10.5194/acp-15-11433-2015>, 2015.
- 11 Jeong, D., Seco, R., Emmons, L., Schwantes, R., Liu, Y., McKinney, K. A., Martin, S. T., Keutsch, F. N., Gu,
12 D., Guenther, A. B., Vega, O., Tota, J., Souza, R. A. F., Springston, S. R., Watson, T. B., and Kim, S.:
13 Reconciling Observed and Predicted Tropical Rainforest OH Concentrations, *JGR Atmospheres*, 127,
14 <https://doi.org/10.1029/2020JD032901>, 2022.
- 15 Kaiser, J., Skog, K. M., Baumann, K., Bertman, S. B., Brown, S. B., Brune, W. H., Crouse, J. D., de Gouw,
16 J. A., Edgerton, E. S., Feiner, P. A., Goldstein, A. H., Koss, A., Misztal, P. K., Nguyen, T. B., Olson, K. F., St.
17 Clair, J. M., Teng, A. P., Toma, S., Wennberg, P. O., Wild, R. J., Zhang, L., and Keutsch, F. N.: Speciation
18 of OH reactivity above the canopy of an isoprene-dominated forest, *Atmos. Chem. Phys.*, 16, 9349–
19 9359, <https://doi.org/10.5194/acp-16-9349-2016>, 2016.
- 20 Kanaya, Y., Cao, R., Akimoto, H., Fukuda, M., Komazaki, Y., Yokouchi, Y., Koike, M., Tanimoto, H.,
21 Takegawa, N., and Kondo, Y.: Urban photochemistry in central Tokyo: 1. Observed and modeled OH
22 and HO₂ radical concentrations during the winter and summer of 2004, *J. Geophys. Res.*, 112, D21312,
23 <https://doi.org/10.1029/2007JD008670>, 2007.
- 24 Kukui, A., Legrand, M., Preunkert, S., Frey, M. M., Loisil, R., Gil Roca, J., Jourdain, B., King, M. D., France,
25 J. L., and Ancellet, G.: Measurements of OH and RO₂ radicals at Dome C, East Antarctica, *Atmospheric*
26 *Chemistry and Physics*, 14, 12373–12392, <https://doi.org/10.5194/acp-14-12373-2014>, 2014.
- 27 Kuyper, B., Wingrove, H., Lesch, T., Labuschagne, C., Say, D., Martin, D., Young, D., Khan, M. A. H.,
28 O'Doherty, S., Davies-Coleman, M. T., and Shallcross, D. E.: Atmospheric Toluene and Benzene Mole
29 Fractions at Cape Town and Cape Point and an Estimation of the Hydroxyl Radical Concentrations in
30 the Air above the Cape Peninsula, South Africa, *ACS Earth Space Chem.*, 4, 24–34,
31 <https://doi.org/10.1021/acsearthspacechem.9b00207>, 2020.
- 32 Lelieveld, J., Butler, T. M., Crowley, J. N., Dillon, T. J., Fischer, H., Ganzeveld, L., Harder, H., Lawrence,
33 M. G., Martinez, M., Taraborrelli, D., and Williams, J.: Atmospheric oxidation capacity sustained by a
34 tropical forest, *Nature*, 452, 737–740, <https://doi.org/10.1038/nature06870>, 2008.
- 35 Lew, M. M., Rickly, P. S., Bottorff, B. P., Reidy, E., Sklaveniti, S., Léonardis, T., Locoge, N., Dusanter, S.,
36 Kundu, S., Wood, E., and Stevens, P. S.: OH and HO₂ radical chemistry in a midlatitude forest:

- 1 measurements and model comparisons, *Atmospheric Chemistry and Physics*, 20, 9209–9230,
2 <https://doi.org/10.5194/acp-20-9209-2020>, 2020.
- 3 Li, Z., Xue, L., Yang, X., Zha, Q., Tham, Y. J., Yan, C., Louie, P. K. K., Luk, C. W. Y., Wang, T., and Wang,
4 W.: Oxidizing capacity of the rural atmosphere in Hong Kong, Southern China, *Science of The Total
5 Environment*, 612, 1114–1122, <https://doi.org/10.1016/j.scitotenv.2017.08.310>, 2018.
- 6 Lou, S., Holland, F., Rohrer, F., Lu, K., Bohn, B., Brauers, T., Chang, C. C., Fuchs, H., Häsel, R., Kita, K.,
7 Kondo, Y., Li, X., Shao, M., Zeng, L., Wahner, A., Zhang, Y., Wang, W., and Hofzumahaus, A.:
8 Atmospheric OH reactivities in the Pearl River Delta – China in summer 2006: measurement and model
9 results, *Atmos. Chem. Phys.*, 10, 11243–11260, <https://doi.org/10.5194/acp-10-11243-2010>, 2010.
- 10 Lu, K., Guo, S., Tan, Z., Wang, H., Shang, D., Liu, Y., Li, X., Wu, Z., Hu, M., and Zhang, Y.: Exploring
11 atmospheric free-radical chemistry in China: the self-cleansing capacity and the formation of
12 secondary air pollution, *National Science Review*, 6, 579–594, <https://doi.org/10.1093/nsr/nwy073>,
13 2019.
- 14 Lu, K. D., Rohrer, F., Holland, F., Fuchs, H., Bohn, B., Brauers, T., Chang, C. C., Häsel, R., Hu, M., Kita,
15 K., Kondo, Y., Li, X., Lou, S. R., Nehr, S., Shao, M., Zeng, L. M., Wahner, A., Zhang, Y. H., and
16 Hofzumahaus, A.: Observation and modelling of OH and HO₂ concentrations in the Pearl River Delta
17 2006: a missing OH source in a VOC rich atmosphere, *Atmospheric Chemistry and Physics*, 12, 1541–
18 1569, <https://doi.org/10.5194/acp-12-1541-2012>, 2012.
- 19 Lu, K. D., Hofzumahaus, A., Holland, F., Bohn, B., Brauers, T., Fuchs, H., Hu, M., Häsel, R., Kita, K.,
20 Kondo, Y., Li, X., Lou, S. R., Oebel, A., Shao, M., Zeng, L. M., Wahner, A., Zhu, T., Zhang, Y. H., and
21 Rohrer, F.: Missing OH source in a suburban environment near Beijing: observed and modelled OH
22 and HO₂ concentrations in summer 2006, *Atmospheric Chemistry and Physics*, 13, 1057–1080,
23 <https://doi.org/10.5194/acp-13-1057-2013>, 2013.
- 24 Ma, X., Tan, Z., Lu, K., Yang, X., Liu, Y., Li, S., Li, X., Chen, S., Novelli, A., Cho, C., Zeng, L., Wahner, A.,
25 and Zhang, Y.: Winter photochemistry in Beijing: Observation and model simulation of OH and HO₂
26 radicals at an urban site, *Science of The Total Environment*, 685, 85–95,
27 <https://doi.org/10.1016/j.scitotenv.2019.05.329>, 2019.
- 28 Mao, J., Ren, X., Zhang, L., Van Duin, D. M., Cohen, R. C., Park, J.-H., Goldstein, A. H., Paulot, F., Beaver,
29 M. R., Crouse, J. D., Wennberg, P. O., DiGangi, J. P., Henry, S. B., Keutsch, F. N., Park, C., Schade, G.
30 W., Wolfe, G. M., Thornton, J. A., and Brune, W. H.: Insights into hydroxyl measurements and
31 atmospheric oxidation in a California forest, *Atmos. Chem. Phys.*, 12, 8009–8020,
32 <https://doi.org/10.5194/acp-12-8009-2012>, 2012.
- 33 Mauldin III, R., Kosciuch, E., Eisele, F., Huey, G., Tanner, D., Sjostedt, S., Blake, D., Chen, G., Crawford,
34 J., and Davis, D.: South Pole Antarctica observations and modeling results: New insights on HO_x radical
35 and sulfur chemistry, *Atmospheric Environment*, 44, 572–581,
36 <https://doi.org/10.1016/j.atmosenv.2009.07.058>, 2010.
- 37 Mauldin III, R. L., Eisele, F. L., Cantrell, C. A., Kosciuch, E., Ridley, B. A., Lefer, B., Tanner, D. J., Nowak, J.

- 1 B., Chen, G., Wang, L., and Davis, D.: Measurements of OH aboard the NASA P-3 during PEM-Tropics
2 B, *J. Geophys. Res.*, 106, 32657–32666, <https://doi.org/10.1029/2000JD900832>, 2001.
- 3 McKeen, S. A., Mount, G., Eisele, F., Williams, E., Harder, J., Goldan, P., Kuster, W., Liu, S. C., Baumann,
4 K., Tanner, D., Fried, A., Sewell, S., Cantrell, C., and Shetter, R.: Photochemical modeling of hydroxyl
5 and its relationship to other species during the Tropospheric OH Photochemistry Experiment, *J.*
6 *Geophys. Res.*, 102, 6467–6493, <https://doi.org/10.1029/96JD03322>, 1997.
- 7 Nie, W., Yan, C., Huang, D. D., Wang, Z., Liu, Y., Qiao, X., Guo, Y., Tian, L., Zheng, P., Xu, Z., Li, Y., Xu,
8 Z., Qi, X., Sun, P., Wang, J., Zheng, F., Li, X., Yin, R., Dallenbach, K. R., Bianchi, F., Petäjä, T., Zhang, Y.,
9 Wang, M., Schervish, M., Wang, S., Qiao, L., Wang, Q., Zhou, M., Wang, H., Yu, C., Yao, D., Guo, H., Ye,
10 P., Lee, S., Li, Y. J., Liu, Y., Chi, X., Kerminen, V.-M., Ehn, M., Donahue, N. M., Wang, T., Huang, C.,
11 Kulmala, M., Worsnop, D., Jiang, J., and Ding, A.: Secondary organic aerosol formed by condensing
12 anthropogenic vapours over China's megacities, *Nat. Geosci.*, 15, 255–261,
13 <https://doi.org/10.1038/s41561-022-00922-5>, 2022.
- 14 Novelli, A., Hens, K., Tatum Ernest, C., Kubistin, D., Regelin, E., Elste, T., Plass-Dülmer, C., Martinez, M.,
15 Lelieveld, J., and Harder, H.: Characterisation of an inlet pre-injector laser-induced fluorescence
16 instrument for the measurement of atmospheric hydroxyl radicals, *Atmos. Meas. Tech.*, 7, 3413–3430,
17 <https://doi.org/10.5194/amt-7-3413-2014>, 2014.
- 18 Novelli, A., Vereecken, L., Bohn, B., Dorn, H.-P., Gkatzelis, G. I., Hofzumahaus, A., Holland, F., Reimer,
19 D., Rohrer, F., Rosanka, S., Taraborrelli, D., Tillmann, R., Wegener, R., Yu, Z., Kiendler-Scharr, A., Wahner,
20 A., and Fuchs, H.: Importance of isomerization reactions for OH radical regeneration from the photo-
21 oxidation of isoprene investigated in the atmospheric simulation chamber SAPHIR, *Atmos. Chem.*
22 *Phys.*, 20, 3333–3355, <https://doi.org/10.5194/acp-20-3333-2020>, 2020.
- 23 Peeters, J. and Müller, J.-F.: HO_x radical regeneration in isoprene oxidation via peroxy radical
24 isomerisations. II: experimental evidence and global impact, *Phys. Chem. Chem. Phys.*, 12, 14227,
25 <https://doi.org/10.1039/c0cp00811g>, 2010.
- 26 Peeters, J., Nguyen, T. L., and Vereecken, L.: HO_x radical regeneration in the oxidation of isoprene,
27 *Phys. Chem. Chem. Phys.*, 11, 5935, <https://doi.org/10.1039/b908511d>, 2009.
- 28 Peeters, J., Müller, J.-F., Stavrou, T., and Nguyen, V. S.: Hydroxyl Radical Recycling in Isoprene
29 Oxidation Driven by Hydrogen Bonding and Hydrogen Tunneling: The Upgraded LIM1 Mechanism, *J.*
30 *Phys. Chem. A*, 118, 8625–8643, <https://doi.org/10.1021/jp5033146>, 2014.
- 31 Peng, X., Wang, T., Wang, W., Ravishankara, A. R., George, C., Xia, M., Cai, M., Li, Q., Salvador, C. M.,
32 Lau, C., Lyu, X., Poon, C. N., Mellouki, A., Mu, Y., Hallquist, M., Saiz-Lopez, A., Guo, H., Herrmann, H.,
33 Yu, C., Dai, J., Wang, Y., Wang, X., Yu, A., Leung, K., Lee, S., and Chen, J.: Photodissociation of particulate
34 nitrate as a source of daytime tropospheric Cl₂, *Nat Commun*, 13, 939,
35 <https://doi.org/10.1038/s41467-022-28383-9>, 2022.
- 36 Rohrer, F., Lu, K., Hofzumahaus, A., Bohn, B., Brauers, T., Chang, C.-C., Fuchs, H., Häseler, R., Holland,
37 F., Hu, M., Kita, K., Kondo, Y., Li, X., Lou, S., Oebel, A., Shao, M., Zeng, L., Zhu, T., Zhang, Y., and Wahner,

- 1 A.: Maximum efficiency in the hydroxyl-radical-based self-cleansing of the troposphere, *Nature*
2 *Geosci*, 7, 559–563, <https://doi.org/10.1038/ngeo2199>, 2014.
- 3 Shirley, T. R., Brune, W. H., Ren, X., Mao, J., Leshner, R., Cardenas, B., Volkamer, R., Molina, L. T., Molina,
4 M. J., Lamb, B., Velasco, E., Jobson, T., and Alexander, M.: Atmospheric oxidation in the Mexico City
5 Metropolitan Area (MCMA) during April 2003, *Atmos. Chem. Phys.*, 13, 2006.
- 6 da Silva, G., Graham, C., and Wang, Z.-F.: Unimolecular β -Hydroxyperoxy Radical Decomposition with
7 OH Recycling in the Photochemical Oxidation of Isoprene, *Environ. Sci. Technol.*, 44, 250–256,
8 <https://doi.org/10.1021/es900924d>, 2010.
- 9 Slater, E. J., Whalley, L. K., Woodward-Massey, R., Ye, C., Lee, J. D., Squires, F., Hopkins, J. R., Dunmore,
10 R. E., Shaw, M., Hamilton, J. F., Lewis, A. C., Crilley, L. R., Kramer, L., Bloss, W., Vu, T., Sun, Y., Xu, W.,
11 Yue, S., Ren, L., Acton, W. J. F., Hewitt, C. N., Wang, X., Fu, P., and Heard, D. E.: Elevated levels of OH
12 observed in haze events during wintertime in central Beijing, *Atmospheric Chemistry and Physics*, 20,
13 14847–14871, <https://doi.org/10.5194/acp-20-14847-2020>, 2020.
- 14 Sommariva, R., Lewis, A. C., Pilling, M. J., and Zador, J.: OH and HO₂ chemistry in clean marine air
15 during SOAPEX-2, *Atmos. Chem. Phys.*, 18, 2004.
- 16 Stone, D., Evans, M. J., Edwards, P. M., Commane, R., Ingham, T., Rickard, A. R., Brookes, D. M., Hopkins,
17 J., Leigh, R. J., Lewis, A. C., Monks, P. S., Oram, D., Reeves, C. E., Stewart, D., and Heard, D. E.: Isoprene
18 oxidation mechanisms: measurements and modelling of OH and HO₂ over a South-East Asian tropical
19 rainforest during the OP3 field campaign, *Atmospheric Chemistry and Physics*, 11, 6749–6771,
20 <https://doi.org/10.5194/acp-11-6749-2011>, 2011.
- 21 Stone, D., Whalley, L. K., and Heard, D. E.: Tropospheric OH and HO₂ radicals: field measurements and
22 model comparisons, *Chem. Soc. Rev.*, 41, 6348, <https://doi.org/10.1039/c2cs35140d>, 2012.
- 23 Tan, D., Faloon, I., Simpas, J. B., Brune, W., Shepson, P. B., Couch, T. L., Sumner, A. L., Carroll, M. A.,
24 Thornberry, T., Apel, E., Riemer, D., and Stockwell, W.: HO_x budgets in a deciduous forest: Results from
25 the PROPHET summer 1998 campaign, *J. Geophys. Res.*, 106, 24407–24427,
26 <https://doi.org/10.1029/2001JD900016>, 2001.
- 27 Tan, Z., Fuchs, H., Lu, K., Hofzumahaus, A., Bohn, B., Broch, S., Dong, H., Gomm, S., Häsel, R., He, L.,
28 Holland, F., Li, X., Liu, Y., Lu, S., Rohrer, F., Shao, M., Wang, B., Wang, M., Wu, Y., Zeng, L., Zhang, Y.,
29 Wahner, A., and Zhang, Y.: Radical chemistry at a rural site (Wangdu) in the North China Plain:
30 observation and model calculations of OH, HO₂ and RO₂ radicals, *Atmospheric Chemistry and Physics*,
31 17, 663–690, <https://doi.org/10.5194/acp-17-663-2017>, 2017.
- 32 Tan, Z., Rohrer, F., Lu, K., Ma, X., Bohn, B., Broch, S., Dong, H., Fuchs, H., Gkatzelis, G. I., Hofzumahaus,
33 A., Holland, F., Li, X., Liu, Y., Liu, Y., Novelli, A., Shao, M., Wang, H., Wu, Y., Zeng, L., Hu, M., Kiendler-
34 Scharr, A., Wahner, A., and Zhang, Y.: Wintertime photochemistry in Beijing: observations of RO_x
35 radical concentrations in the North China Plain during the BEST-ONE campaign, *Atmospheric*
36 *Chemistry and Physics*, 18, 12391–12411, <https://doi.org/10.5194/acp-18-12391-2018>, 2018.

- 1 Tan, Z., Lu, K., Hofzumahaus, A., Fuchs, H., Bohn, B., Holland, F., Liu, Y., Rohrer, F., Shao, M., Sun, K.,
2 Wu, Y., Zeng, L., Zhang, Y., Zou, Q., Kiendler-Scharr, A., Wahner, A., and Zhang, Y.: Experimental
3 budgets of OH, HO₂, and RO₂ radicals and implications for ozone formation in the Pearl River Delta
4 in China 2014, *Atmospheric Chemistry and Physics*, 19, 7129–7150, [https://doi.org/10.5194/acp-19-](https://doi.org/10.5194/acp-19-7129-2019)
5 7129-2019, 2019.
- 6 Tang, J. H., Chan, L. Y., Chan, C. Y., Li, Y. S., Chang, C. C., Wang, X. M., Zou, S. C., Barletta, B., Blake, D.
7 R., and Wu, D.: Implications of changing urban and rural emissions on non-methane hydrocarbons in
8 the Pearl River Delta region of China, *Atmospheric Environment*, 42, 3780–3794,
9 <https://doi.org/10.1016/j.atmosenv.2007.12.069>, 2008.
- 10 Tanner, D. J. and Eisele, F. L.: Present OH measurement limits and associated uncertainties, *J. Geophys.*
11 *Res.*, 100, 2883, <https://doi.org/10.1029/94JD02609>, 1995.
- 12 Tanner, D. J., Jefferson, A., and Eisele, F. L.: Selected ion chemical ionization mass spectrometric
13 measurement of OH, *J. Geophys. Res.*, 102, 6415–6425, <https://doi.org/10.1029/96JD03919>, 1997.
- 14 Thames, A. B., Brune, W. H., Miller, D. O., Allen, H. M., Apel, E. C., Blake, D. R., Bui, T. P., Commane, R.,
15 Crouse, J. D., Daube, B. C., Diskin, G. S., DiGangi, J. P., Elkins, J. W., Hall, S. R., Hanisco, T. F., Hannun,
16 R. A., Hints, E., Hornbrook, R. S., Kim, M. J., McKain, K., Moore, F. L., Nicely, J. M., Peischl, J., Ryerson,
17 T. B., St. Clair, J. M., Sweeney, C., Teng, A., Thompson, C. R., Ullmann, K., Wennberg, P. O., and Wolfe,
18 G. M.: Missing OH reactivity in the global marine boundary layer, *Atmospheric Chemistry and Physics*,
19 20, 4013–4029, <https://doi.org/10.5194/acp-20-4013-2020>, 2020.
- 20 Walker, H. L., Heal, M. R., Braban, C. F., Whalley, L. K., and Twigg, M. M.: Evaluation of local
21 measurement-driven adjustments of modelled cloud-free atmospheric photolysis rate coefficients,
22 *Environ. Sci.: Atmos.*, 2, 1411–1427, <https://doi.org/10.1039/D2EA00072E>, 2022.
- 23 Wang, F., Hu, R., Chen, H., Xie, P., Wang, Y., Li, Z., Jin, H., Liu, J., and Liu, W.: Development of a field
24 system for measurement of tropospheric OH radical using laser-induced fluorescence technique, *Opt.*
25 *Express*, 27, A419, <https://doi.org/10.1364/OE.27.00A419>, 2019a.
- 26 Wang, G., Iradukunda, Y., Shi, G., Sanga, P., Niu, X., and Wu, Z.: Hydroxyl, hydroperoxyl free radicals
27 determination methods in atmosphere and troposphere, *Journal of Environmental Sciences*, 99, 324–
28 335, <https://doi.org/10.1016/j.jes.2020.06.038>, 2021a.
- 29 Wang, T., Dai, J., Lam, K. S., Nan Poon, C., and Brasseur, G. P.: Twenty-Five Years of Lower Tropospheric
30 Ozone Observations in Tropical East Asia: The Influence of Emissions and Weather Patterns,
31 *Geophysical Research Letters*, 46, 11463–11470, <https://doi.org/10.1029/2019GL084459>, 2019b.
- 32 Wang, Y., Hu, R., Xie, P., Chen, H., Wang, F., Liu, X., Liu, J., and Liu, W.: Measurement of tropospheric
33 HO₂ radical using fluorescence assay by gas expansion with low interferences, *Journal of*
34 *Environmental Sciences*, 99, 40–50, <https://doi.org/10.1016/j.jes.2020.06.010>, 2021b.
- 35 Wang, Y. Q.: MeteolInfo: GIS software for meteorological data visualization and analysis:
36 *Meteorological GIS software*, *Met. Apps*, 21, 360–368, <https://doi.org/10.1002/met.1345>, 2014.

- 1 Wang, Y. Q.: An Open Source Software Suite for Multi-Dimensional Meteorological Data Computation
2 and Visualisation, *JORS*, 7, 21, <https://doi.org/10.5334/jors.267>, 2019.
- 3 Whalley, L. K., Edwards, P. M., Furneaux, K. L., Goddard, A., Ingham, T., Evans, M. J., Stone, D., Hopkins,
4 J. R., Jones, C. E., Karunaharan, A., Lee, J. D., Lewis, A. C., Monks, P. S., Moller, S. J., and Heard, D. E.:
5 Quantifying the magnitude of a missing hydroxyl radical source in a tropical rainforest, *Atmos. Chem.*
6 *Phys.*, 11, 7223–7233, <https://doi.org/10.5194/acp-11-7223-2011>, 2011.
- 7 Whalley, L. K., Stone, D., Dunmore, R., Hamilton, J., Hopkins, J. R., Lee, J. D., Lewis, A. C., Williams, P.,
8 Kleffmann, J., Laufs, S., Woodward-Massey, R., and Heard, D. E.: Understanding in situ ozone
9 production in the summertime through radical observations and modelling studies during the Clean
10 air for London project (ClearfLo), *Atmos. Chem. Phys.*, 18, 2547–2571, [https://doi.org/10.5194/acp-](https://doi.org/10.5194/acp-18-2547-2018)
11 [18-2547-2018](https://doi.org/10.5194/acp-18-2547-2018), 2018.
- 12 Wolfe, G. M., Marvin, M. R., Roberts, S. J., Travis, K. R., and Liao, J.: The Framework for 0-D Atmospheric
13 Modeling (F0AM) v3.1, *Geosci. Model Dev.*, 9, 3309–3319, <https://doi.org/10.5194/gmd-9-3309-2016>,
14 2016.
- 15 Woodward-Massey, R., Slater, E. J., Alen, J., Ingham, T., Cryer, D. R., Stimpson, L. M., Ye, C., Seakins, P.
16 W., Whalley, L. K., and Heard, D. E.: Implementation of a chemical background method for
17 atmospheric OH measurements by laser-induced fluorescence: characterisation and observations
18 from the UK and China, *Atmospheric Measurement Techniques*, 13, 3119–3146,
19 <https://doi.org/10.5194/amt-13-3119-2020>, 2020.
- 20 Xia, M., Wang, T., Wang, Z., Chen, Y., Peng, X., Huo, Y., Wang, W., Yuan, Q., Jiang, Y., Guo, H., Lau, C.,
21 Leung, K., Yu, A., and Lee, S.: Pollution-Derived Br₂ Boosts Oxidation Power of the Coastal Atmosphere,
22 *Environ. Sci. Technol.*, 56, 12055–12065, <https://doi.org/10.1021/acs.est.2c02434>, 2022.
- 23 Xiao, Y., Jacob, D. J., and Turquety, S.: Atmospheric acetylene and its relationship with CO as an
24 indicator of air mass age, *J. Geophys. Res.*, 112, D12305, <https://doi.org/10.1029/2006JD008268>, 2007.
- 25 Yang, X., Lu, K., Ma, X., Gao, Y., Tan, Z., Wang, H., Chen, X., Li, X., Huang, X., He, L., Tang, M., Zhu, B.,
26 Chen, S., Dong, H., Zeng, L., and Zhang, Y.: Radical chemistry in the Pearl River Delta: observations
27 and modeling of OH and HO₂ radicals in Shenzhen 2018, *Atmospheric Chemistry and Physics*
28 *Discussions*, 1–19, <https://doi.org/10.5194/acp-2022-113>, 2022.
- 29 Yang, Y., Shao, M., Wang, X., Nölscher, A. C., Kessel, S., Guenther, A., and Williams, J.: Towards a
30 quantitative understanding of total OH reactivity: A review, *Atmospheric Environment*, 134, 147–161,
31 <https://doi.org/10.1016/j.atmosenv.2016.03.010>, 2016.
- 32 Yao, T., Fung, J. C. H., Ma, H., Lau, A. K. H., Chan, P. W., Yu, J. Z., and Xue, J.: Enhancement in secondary
33 particulate matter production due to mountain trapping, *Atmospheric Research*, 147–148, 227–236,
34 <https://doi.org/10.1016/j.atmosres.2014.05.007>, 2014.

35

Figures and Tables

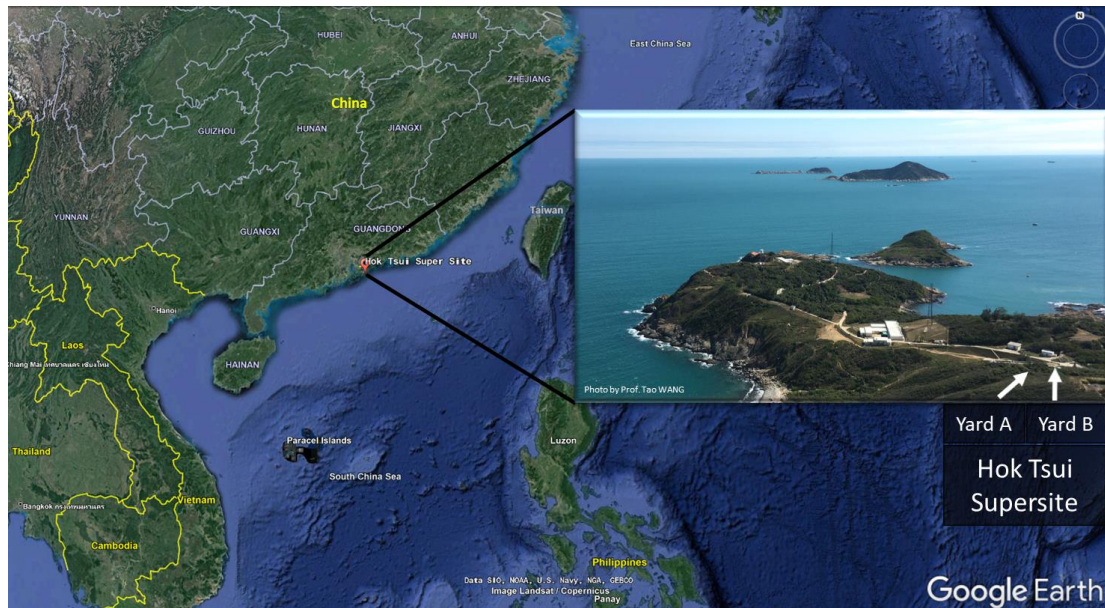


Figure 1. The location of the Hok Tsui Air Monitoring Supersite in Hong Kong, South China.

The map is from © Google Earth.

Table 1. Measuring instruments and measured species in the field campaign

Species	Instruments	Time Resolution	Detection Limit	Accuracy (1σ)
NO, NO ₂	Chemiluminescence/photolytic converter (Thermo, Model 42i)	1 min	60 ppt	NO: $\pm 5.2\%$ NO ₂ : $\pm 15.2\%$
OH	Nitrate-quadrupole chemical ionization mass spectrometer (CIMS)	10 s	Lab: $1.5 \times 10^5 \text{ cm}^{-3}$ Daytime: $1 \times 10^6 \text{ cm}^{-3}$	$\pm 44\%$
Ozone	Ozone analyzer, model 49i, Thermo Scientific	1 min	0.5 ppb	$\pm 6.0\%$
JNO ₂	Filter Radiometer, Metcon	1 min	$4 \times 10^{-5} \text{ s}^{-1}$	$\pm 10\%$
HONO	Iodide-Tof-CIMS, Aerodyne Inc	1s	0.2 ppt	$\pm 15\%$
SO ₂	Pulsed Fluorescence SO ₂ Analyzer (Thermo, Model 43i)	1 min	1 ppb	$\pm 6.1\%$
CO	Gas Filter Correlation CO Analyzer (Thermo, Model 48i)	1 min	40 ppb	$\pm 7.4\%$
NH ₃	Chemiluminescence NH ₃ Analyzer (Thermo, Model 17i)	2 mins	1 ppb	$\pm 8\%$
Particle number size distribution	Scanning mobility particle sizer, TSI	5 mins	1 particle cm^{-3}	$\pm 10\%$
VOCs	GC-MS/FID (GC955 Series 611/811, Syntech Spectras)	1 hour	~ 10 ppt	$\pm 20\%$
	PTR-MS (PTR-QMS 500, IONICON Analytik, Austria)	5 mins	20 ppt	$\pm 20\%$
OVOCs	PTR-Tof-MS, IONICON Analytic;	1 s	~ 10 ppt	$\pm 15\%$

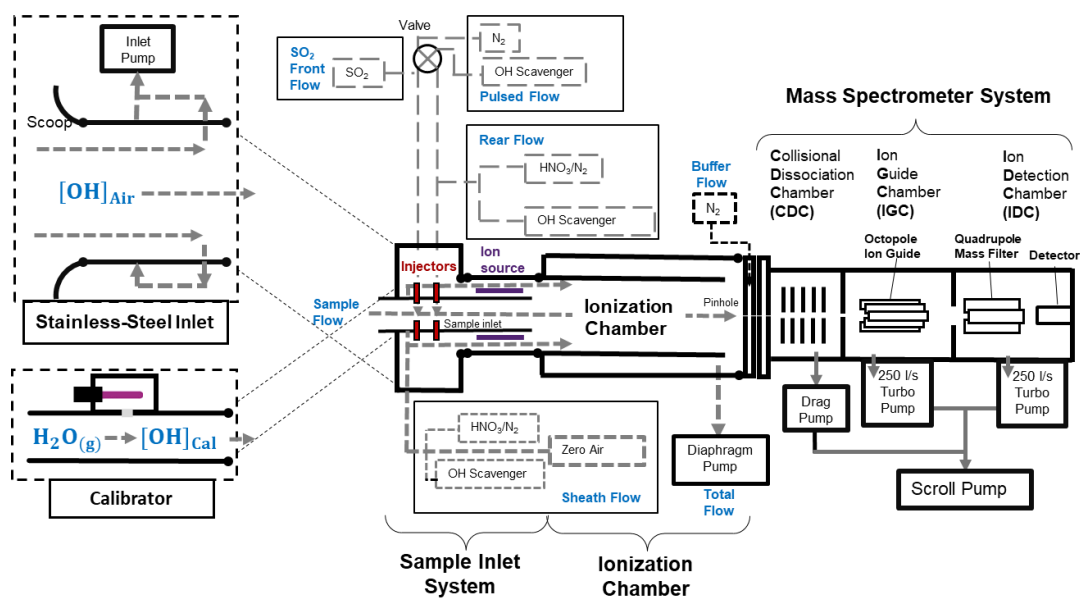


Figure 2. Schematics of the CIMS system which consists of a stainless-steel inlet, a sample inlet, an ionization chamber, a mass spectrometer system, and a calibration unit. The CIMS measures the ambient OH concentration when connecting to the stainless-steel inlet whereas, during calibration, the calibration unit is connected to the CIMS instead. Details of the setup, calibration and optimization of the CIMS can be found in the Supplementary.

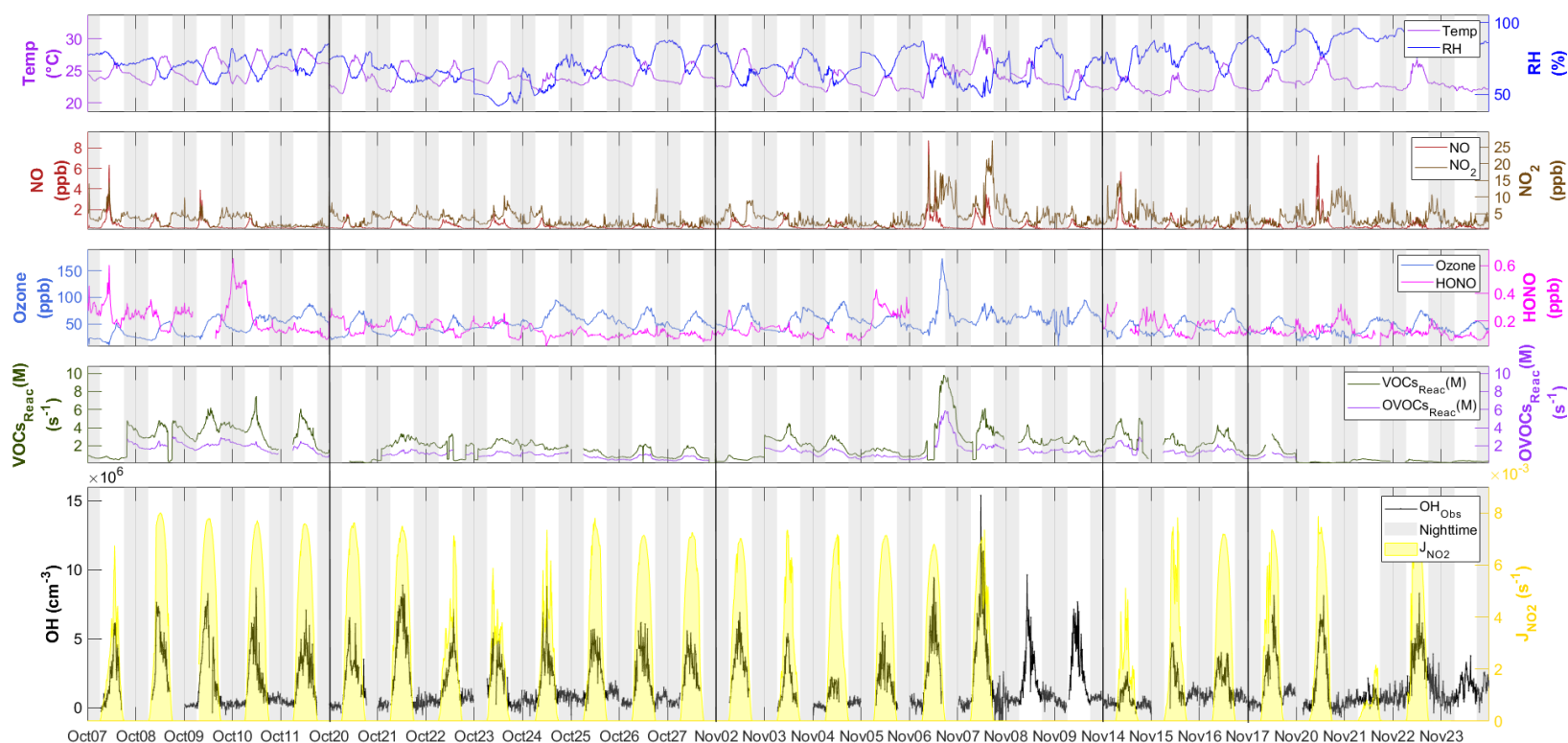
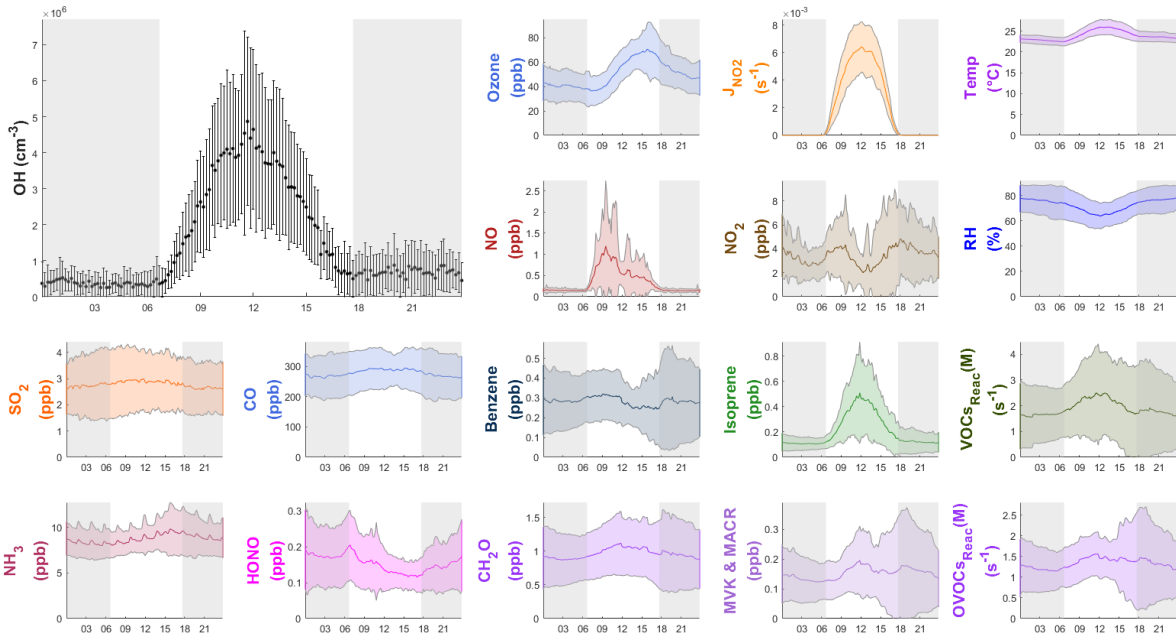
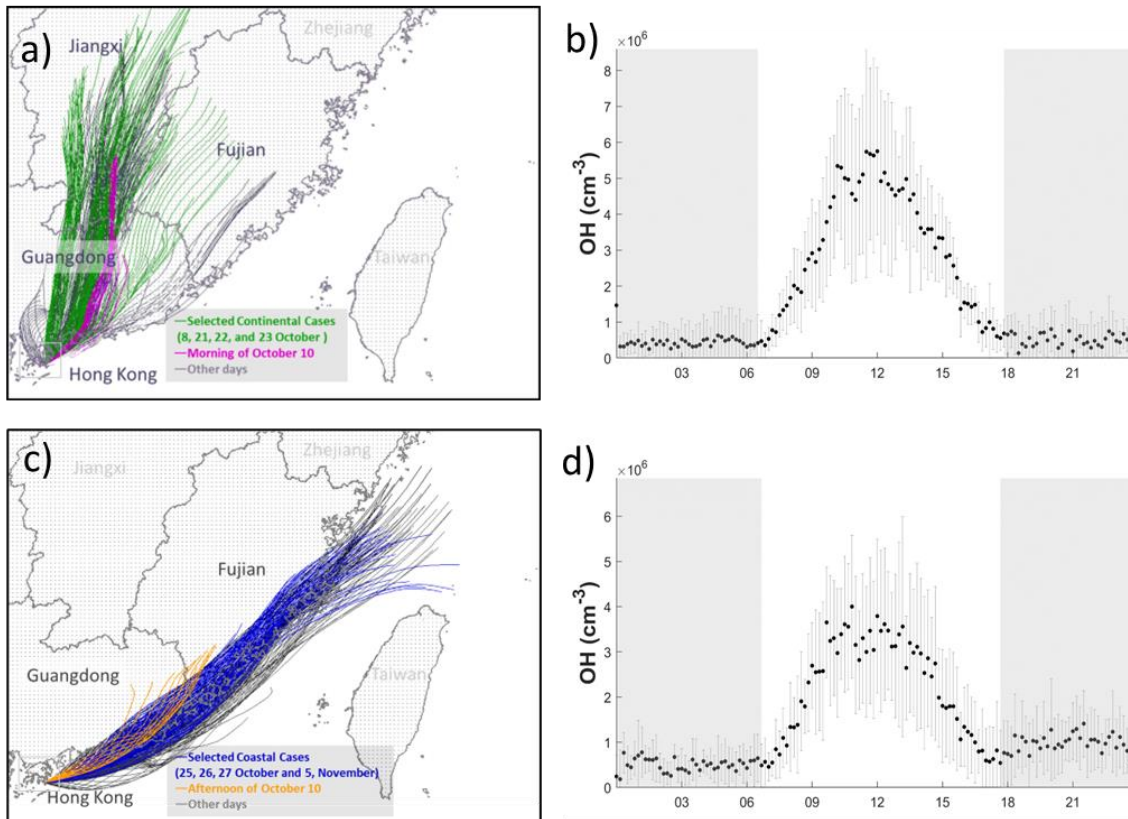


Figure 3. Time series of OH between 7 October and 23 November with measured weather conditions (temperature and RH), OH primary sources (ozone and HONO), NO_x (NO and NO_2), reactivity of measured VOCs and OVOCs ($\text{VOCs}_{\text{Reac}}(\text{M})$ and $\text{OVOCs}_{\text{Reac}}(\text{M})$), and photolysis frequency (J_{NO_2}). All measurement data shown are 10 min averages. The gaps of the data were due to the calibration or instrument maintenance. The black lines separate the non-continuous days during measurement. The grey shaded area denotes night-time. The time zone was local time (+8 UTC) for the x-axis.



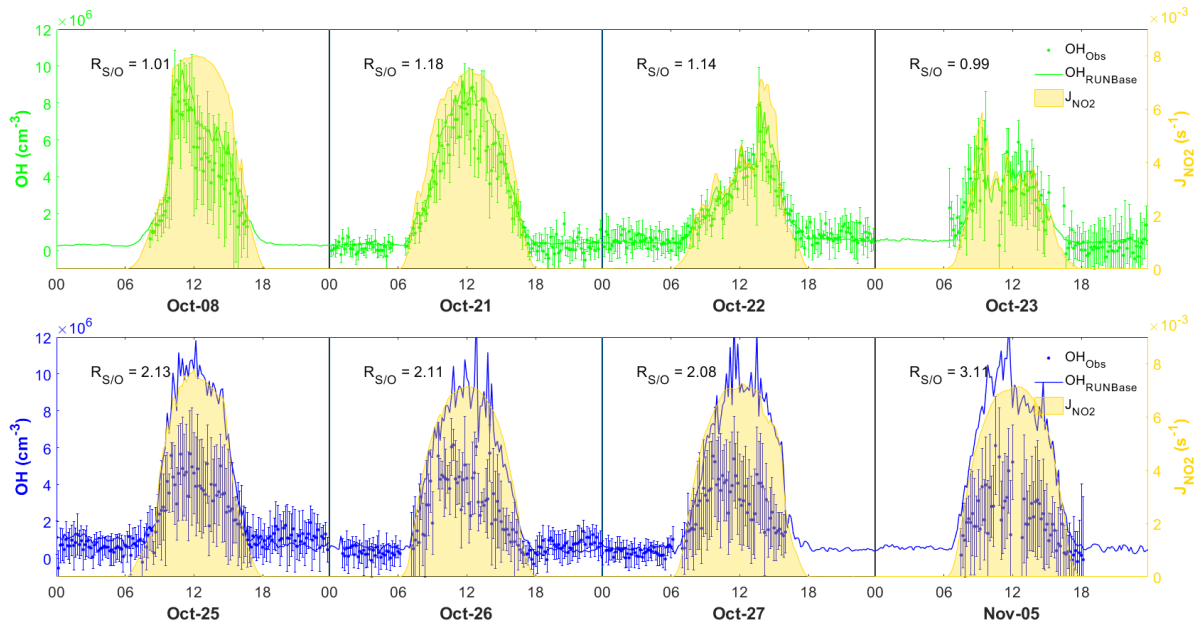
1
 2 Figure 4. Diurnal profiles of the average ($\pm 1\sigma$) concentrations of OH, other chemical species, the
 3 measured VOCs reactivity and OVOCs reactivity ($\text{VOCs}_{\text{Reac}}(\text{M})$ and $\text{OVOCs}_{\text{Reac}}(\text{M})$), and
 4 meteorological parameters (T , RH , J_{NO_2}) during the field campaign. The grey shaded area denotes night-
 5 time. The error bars and shaded error bars are the standard deviation of the averaged data.



6
 7 Figure 5. 24 h back trajectories of the continental (a) and coastal (c) cases over the whole measurement

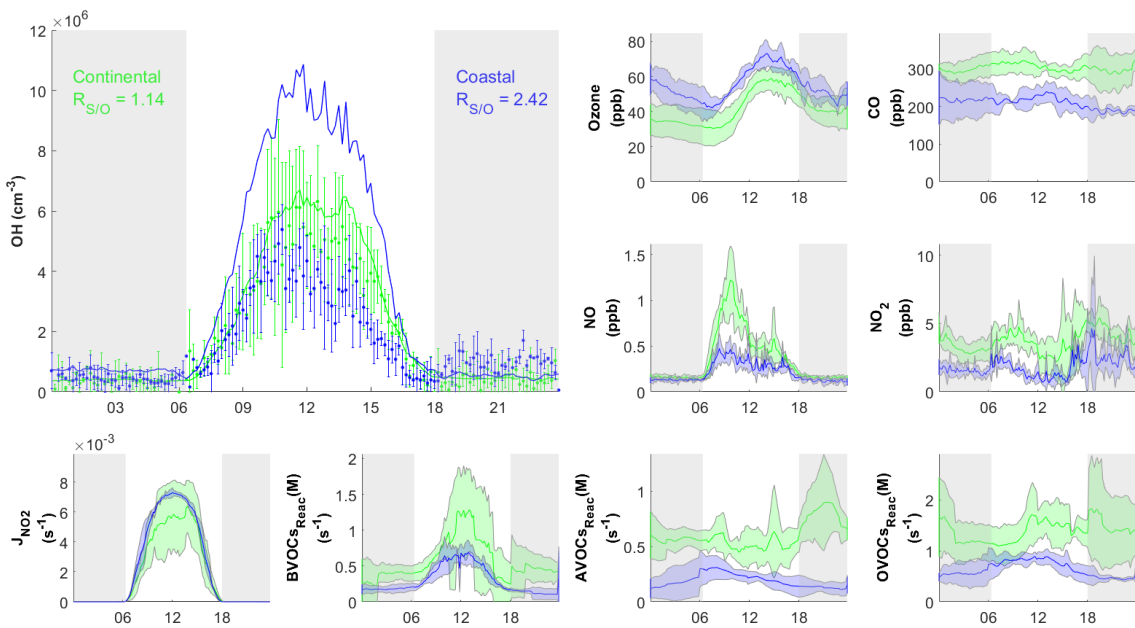
1 period. The selected days for coastal, continental, and mixed cases are labelled in different colours. (b)
 2 and (d) show the average concentration of OH with standard deviation in continental and coastal air
 3 masses, respectively. The error bars and shaded error bars are the standard deviation of the averaged
 4 data.

5



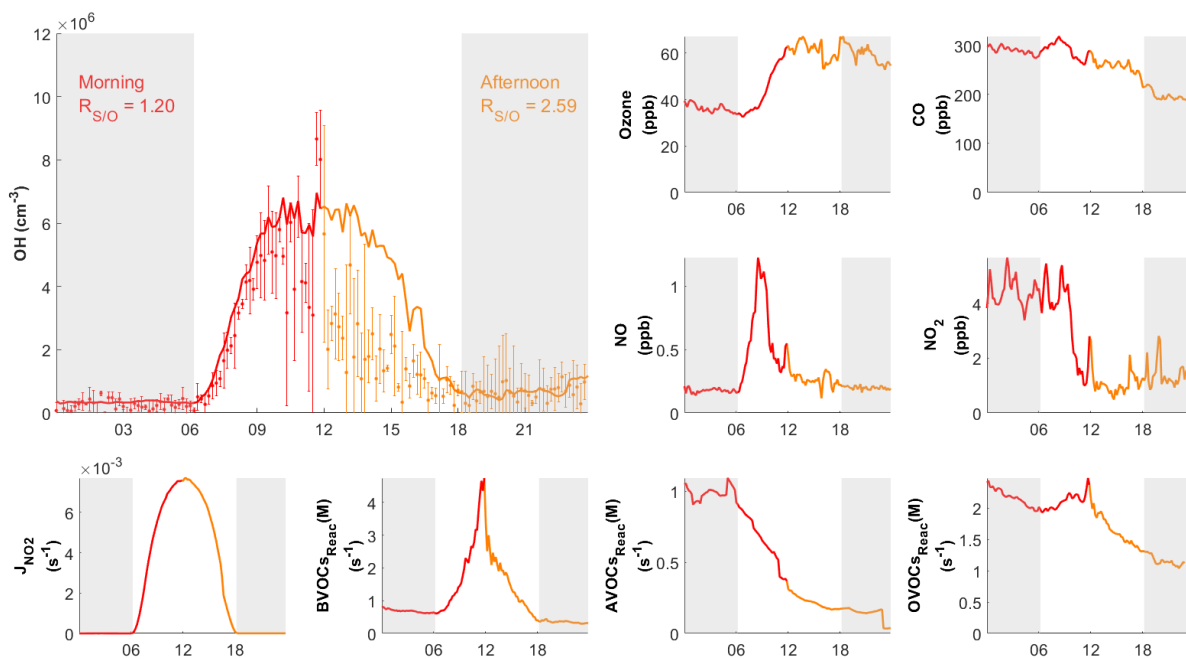
6

7 Figure 6. Comparison between observed (dots) and simulated (lines) OH in the four continental cases
 8 (top panel) and the four coastal cases (lower panel), also showing measurement uncertainty (error bars)
 9 and J_{NO_2} measurement (yellow shades). The time zone was local time (+8 UTC) for the x-axis.

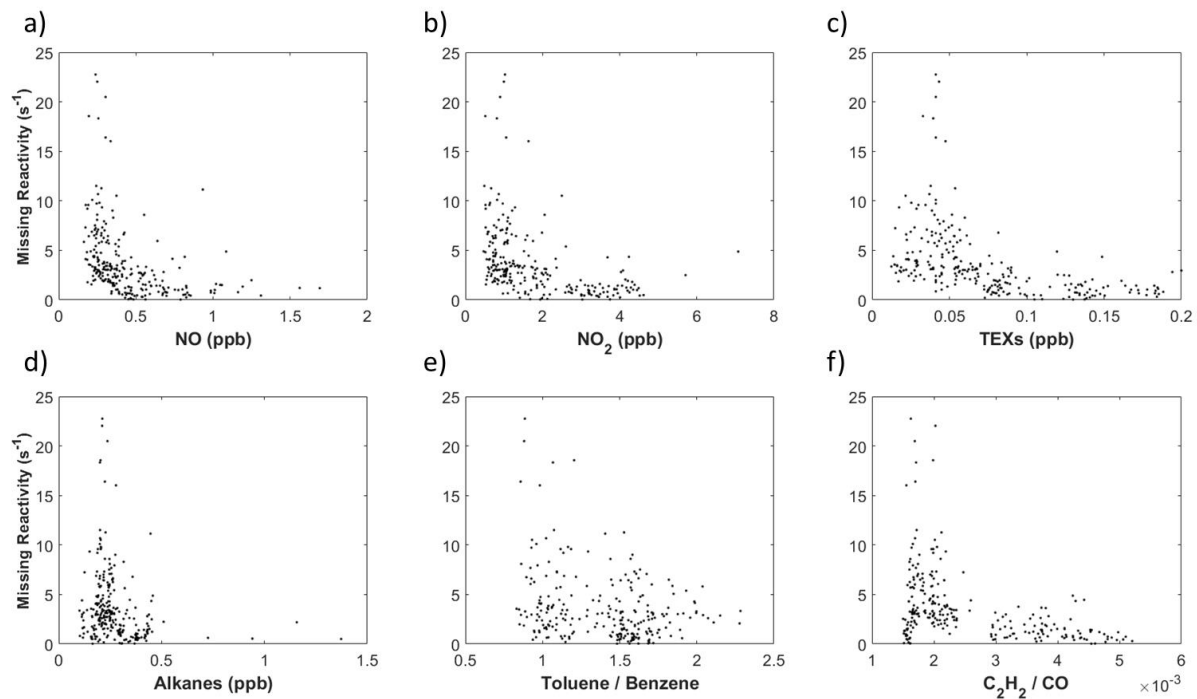


10

1 Figure 7. Diurnal profiles of average concentrations of measured (dots) with standard deviation and
 2 simulated (RUNBase, line) OH concentration, important trace gases and the measured BVOCs, AVOCs,
 3 OVOCs reactivity ($BVOC_{SReac}(M)$, $AVOC_{SReac}(M)$ and $OVOC_{SReac}(M)$) for selected cases in continental
 4 (green) and coastal (blue) air masses. The grey shaded area denotes night-time. The error bars and
 5 shaded error bars are the standard deviation of the averaged data.
 6



7
 8 Figure 8. Diurnal profiles of measured (dots) with measurement uncertainty (error bars) and simulated
 9 (RUNBase, line) OH on 10 October 2020, with other chemical species and the measured BVOCs,
 10 AVOCs, OVOCs reactivity ($BVOC_{SReac}(M)$, $AVOC_{SReac}(M)$ and $OVOC_{SReac}(M)$). The air mass drifted
 11 from continental (red) in the morning to coastal (orange) in the afternoon. The grey shaded area denotes
 12 night-time. The time zone was local time (+8 UTC) for the x-axis.
 13
 14



1
2
3
4
5

Figure 9. The dependence of calculated missing reactivity on a) NO, b) NO₂, c) TEXs (toluene, ethylbenzene, and xylenes), d) alkanes (C₂ to C₈), e) the ratio of toluene to benzene, and f) the ratio of C₂H₂ to CO.